nature nanotechnology

Article

https://doi.org/10.1038/s41565-024-01681-7

Oral mitochondrial transplantation using nanomotors to treat ischaemic heart disease

Received: 20 September 2023

Accepted: 15 April 2024

Published online: 27 May 2024

Check for updates

Ziyu Wu[1,2,4], Lin Chen[1,4], Wenyan Guo[1], Jun Wang[3], Haiya Ni[3], Jianing Liu[3], Wentao Jiang[2], Jian Shen[1], Chun Mao[1] ✉, Min Zhou[2,3] ✉ & Mimi Wan[1] ✉

Mitochondrial transplantation is an important therapeutic strategy for restoring energy supply in patients with ischaemic heart disease (IHD); however, it is limited by the invasiveness of the transplantation method and loss of mitochondrial activity. Here we report successful mitochondrial transplantation by oral administration for IHD therapy. A nitric-oxide-releasing nanomotor is modified on the mitochondria surface to obtain nanomotorized mitochondria with chemotactic targeting ability towards damaged heart tissue due to nanomotor action. The nanomotorized mitochondria are packaged in enteric capsules to protect them from gastric acid erosion. After oral delivery the mitochondria are released in the intestine, where they are quickly absorbed by intestinal cells and secreted into the bloodstream, allowing delivery to the damaged heart tissue. The regulation of disease microenvironment by the nanomotorized mitochondria can not only achieve rapid uptake and high retention of mitochondria by damaged cardiomyocytes but also maintains high activity of the transplanted mitochondria. Furthermore, results from animal models of IHD indicate that the accumulated nanomotorized mitochondria in the damaged heart tissue can regulate cardiac metabolism at the transcriptional level, thus preventing IHD progression. This strategy has the potential to change the therapeutic strategy used to treat IHD.

Ischaemic heart disease (IHD) is the leading cause of death worldwide. The condition is characterized by cardiomyocyte mitochondrial dysfunction and, consequently, energy metabolism disorders[1]. Current therapeutic options for chronic IHD (including mild conditions such as silent myocardial ischaemia) include long-term oral medication (for example, β-blockers (BBs))[2,3]. The recommended treatment for acute IHD (for example, myocardial infarction) is usually surgery (for example, reperfusion), but this may cause additional damage (for example, ischaemia-reperfusion injury (IRI)), and hence many of these patients continue to require long-term or even lifelong medication after surgery[4]. Unfortunately, none of these clinical treatments can recover the normal energy supply to the heart and halt its continuous deterioration[5], but can only alleviate the deterioration. Mitochondrial transplantation has been proposed as a more effective treatment for IHD because the transplanted mitochondria are expected to fuse with the damaged mitochondria in cardiomyocytes[6–8], providing intact respiratory chain proteins and crucial DNA sequences, and thereby halting cardiac deterioration[9]. However, research on transplanting mitochondria into the heart is still in the early stages. Since the first report of mitochondrial transplantation technology in the treatment of the ischaemic

[1]National and Local Joint Engineering Research Center of Biomedical Functional Materials, School of Chemistry and Materials Science, Nanjing Normal University, Nanjing, China. [2]Department of Vascular Surgery, Nanjing Drum Tower Hospital, The Affiliated Hospital of Nanjing University Medical School, Nanjing, China. [3]Department of Vascular Surgery, Nanjing Drum Tower Hospital, Clinical College of Nanjing University of Chinese Medicine, Nanjing, China. [4]These authors contributed equally: Ziyu Wu, Lin Chen. ✉e-mail: maochun@njnu.edu.cn; zhouminnju@nju.edu.cn; wanmimi@njnu.edu.cn

heart of rabbit was published in 2009[10], only about 11 animal studies and two clinical studies have been carried out (detailed information can be found in the illustration below Extended Data Table 1), most of which relied on open-heart surgery (for example, intramyocardial injection) or interventional procedures (for example, intracoronary injection). The high degree of invasiveness of the transplantation method[11] and the difficulty in maintaining donor mitochondrial activity in the pathological environment are key factors limiting the development of this technology[7,12]. Therefore, developing a minimally invasive way to transplant highly active mitochondria is an important but extremely challenging goal.

In light of the long-term and frequent medication needs of patients with IHD, minimally invasive intravenous administration and non-invasive oral administration are considered to be the preferred treatment approaches. In situations where both routes of administration achieve similar therapeutic effects, oral administration is considered to be superior[13]. In this study, we developed a non-invasive method for transplanting mitochondria via the oral route. First, we prepared nanomotorized mitochondria (NM/Mito) that released nitric oxide (NO) and exhibited chemotaxis to cardiac injury sites expressing high levels of inducible nitric oxide synthase (iNOS) and reactive oxygen species (ROS). Subsequently, we added cardiomyocyte membrane (CM) fragments asymmetrically to the surface of NM/Mito to generate CM/NM/Mito (Fig. 1a), which were then loaded into pH-responsive enteric capsules to generate CM/NM/Mito@Cap (body-joint cargo module, CM/NM/Mito; tail-joint power module, sodium bicarbonate and citric acid) for oral administration. CM/NM/Mito@Cap was designed to remain intact in the presence of gastric acid and dissolve in the intestine (Fig. 1b). The rapid reaction between sodium bicarbonate and citric acid in the capsule's power module was intended to generate a large amount of CO_2, providing additional power for breaking through the intestinal mucus barrier. The CM component can promote the rapid endocytosis of mitochondria by intestinal epithelial cells, followed by exocytosis into the bloodstream. Subsequently, CM/NM/Mito delivered to the blood circulation are transported by the chemotaxis of the NM component to the damaged site of the heart, where they are strongly retained in the damaged cardiomyocytes. Selective exocytosis of CM/NM/Mito by intestinal epithelial cells and high retention of CM/NM/Mito by damaged cardiomyocytes are two crucial but highly complex aspects of this process. Meanwhile, CM/NM/Mito will consume ROS and generate NO during the chemotaxis process, regulating the disease microenvironment, and thereby promoting the transplanted mitochondria to fully perform the function of re-establishing energy metabolism.

Biological and chemotactic properties of CM/NM/Mito

Mitochondria were isolated from human umbilical cord mesenchymal stem cells (huMSCs) (Extended Data Fig. 1a). The results of morphology characterization demonstrated successful mitochondrial extraction (Fig. 1c and Extended Data Fig. 1b,c)[14]. Subsequently, the basic unit of the NM component, L-arginine derivative methacrylate (M-Arg), and the ROS-responsive diselenide cross-linker were synthesized and characterized (Extended Data Fig. 1d–g)[15]. NM/Mito was obtained by a free-radical polymerization reaction (Extended Data Fig. 1h). Characterization of the physicochemical properties confirmed the successful mitochondrial modification (Fig. 1d and Extended Data Fig. 1b,c,i,j). Next, CM was used to asymmetrically modify the surface of the NM/Mito by electrostatic interaction, yielding CM/NM/Mito (Extended Data Fig. 2a,b)[16]. The above modification process was confirmed by fluorescence co-localization and characteristic western blotting of the CM proteins (Fig. 1e and Extended Data Fig. 2c). In addition to preserving the original biological functions of mitochondria (Fig. 1f,g and Extended Data Fig. 2d–g)[14,17], CM/NM/Mito were also additionally endowed with ROS-depleting and NO-generating abilities in the damaged cardiomyocytes (H9c2) compared with normal cells (Fig. 1h,i and Extended Data Fig. 2h).

Oxidative stress is an important feature of IHD[18]. The high levels of ROS and iNOS at the lesion site may serve as chemoattractants for CM/NM/Mito[19]. In a Y-channel device (Extended Data Fig. 3a), the fluorescence intensity of CM/NM/Mito increased significantly with time in the reservoir which had a higher ROS/iNOS concentration. These results demonstrated that the CM/NM/Mito actively sensed the high ROS/iNOS concentration and diffused up the concentration gradient (Extended Data Fig. 3b–e and Supplementary Fig. 1). We further evaluated the chemotactic behaviour of the CM/NM/Mito in a dynamic fluidic environment using a Ψ-type microfluidic chip[20] (Extended Data Fig. 3f). Chemotactic displacement of the CM/NM/Mito was determined by comparing the fluorescence intensity distribution perpendicular to the direction of fluid flow. As shown in Extended Data Fig. 3g,h, it can be seen that CM/NM/Mito exhibited chemotaxis in a dynamic fluid environment, an ability that would be necessary for targeting IHD lesion sites.

Cellular uptake and selective exocytosis of CM/NM/Mito

High levels of Cx43 expression in CM mediate the formation of gap junction channels (GJCs) with recipient cells and affect intracellular Ca^{2+} levels[21,22]. It has been reported that GJC formation and related changes in Ca^{2+} levels promote mitochondrial uptake by cells[23]. We hypothesized that GJC formation would promote adhesion of CM/NM/Mito to recipient cells (normal rat intestinal epithelial cells (IEC-6) and H9c2 cells), thus promoting cellular uptake of CM/NM/Mito (Fig. 2a). The results of calcein staining and calcein release assay confirmed that CM/NM/Mito established GJCs with cells (Fig. 2b, Supplementary Fig. 2 and Extended Data Fig. 4a)[24]. GJC formation caused cells to take more CM/NM/Mito than unmodified mitochondria and NM/Mito (Fig. 2c–f and Supplementary Fig. 3). In terms of the main pathways mediating CM/NM/Mito uptake by different cells (Extended Data Fig. 4b), the results were consistent with an earlier study reporting that cell-membrane-modified nanoparticles can fuse with cells homologous to the modified membrane component, whereas membrane fusion is not significant when the membrane component is not homologous to the cell type[25].

Theoretically, normal intestinal epithelial cells that are not expressing high levels of iNOS and ROS can establish GJCs with CM/NM/Mito and efficiently take up CM/NM/Mito[26]. During this process, Ca^{2+} levels increase significantly, which initiates mitochondrial exocytosis[23]. Damaged cardiomyocytes also take up CM/NM/Mito by forming GJCs; however, because of the elevated levels of iNOS and ROS in damaged cardiomyocytes, CM/NM/Mito are expected to release NO when they enter the cells, thereby decreasing cellular Ca^{2+} levels[27], inhibiting CM/NM/Mito exocytosis (Fig. 2g). We demonstrated that intestinal epithelial cells and cardiomyocytes did experience an increase in Ca^{2+} levels during CM/NM/Mito uptake, whereas NO release rapidly reduced Ca^{2+} levels in damaged cells (Fig. 2h,i). Analysis of CM/NM/Mito leakage results showed that 68.9% of the CM/NM/Mito taken up by normal IEC-6 cells were actively excreted (Fig. 2j), whereas damaged IEC-6 cells only excreted 40.5% of the CM/NM/Mito that they took up. This difference was even more pronounced in cardiomyocytes (Fig. 2k): normal H9c2 cells excreted 48.2% of CM/NM/Mito after uptake, whereas damaged H9c2 cells excreted only 13.2%. The ability of CM/NM/Mito to regulate cellular Ca^{2+} levels is important for achieving rapid exocytosis from intestinal epithelial cells and efficient retention by damaged cardiomyocytes.

In terms of the cellular location, the Pearson's *r* values suggested that CM/NM/Mito co-localized with cardiomyocyte mitochondria (Fig. 2l and Supplementary Fig. 4)[28], indicating that the transplanted mitochondria fused with the endogenous mitochondria. As shown in Extended Data Fig. 4c,d, the mitochondria in cells coincubated with CM/NM/Mito were elongated and exhibited roundness similar to that of normal mitochondria, both of which are factors that could

https://doi.org/10.1038/s41565-024-01681-7

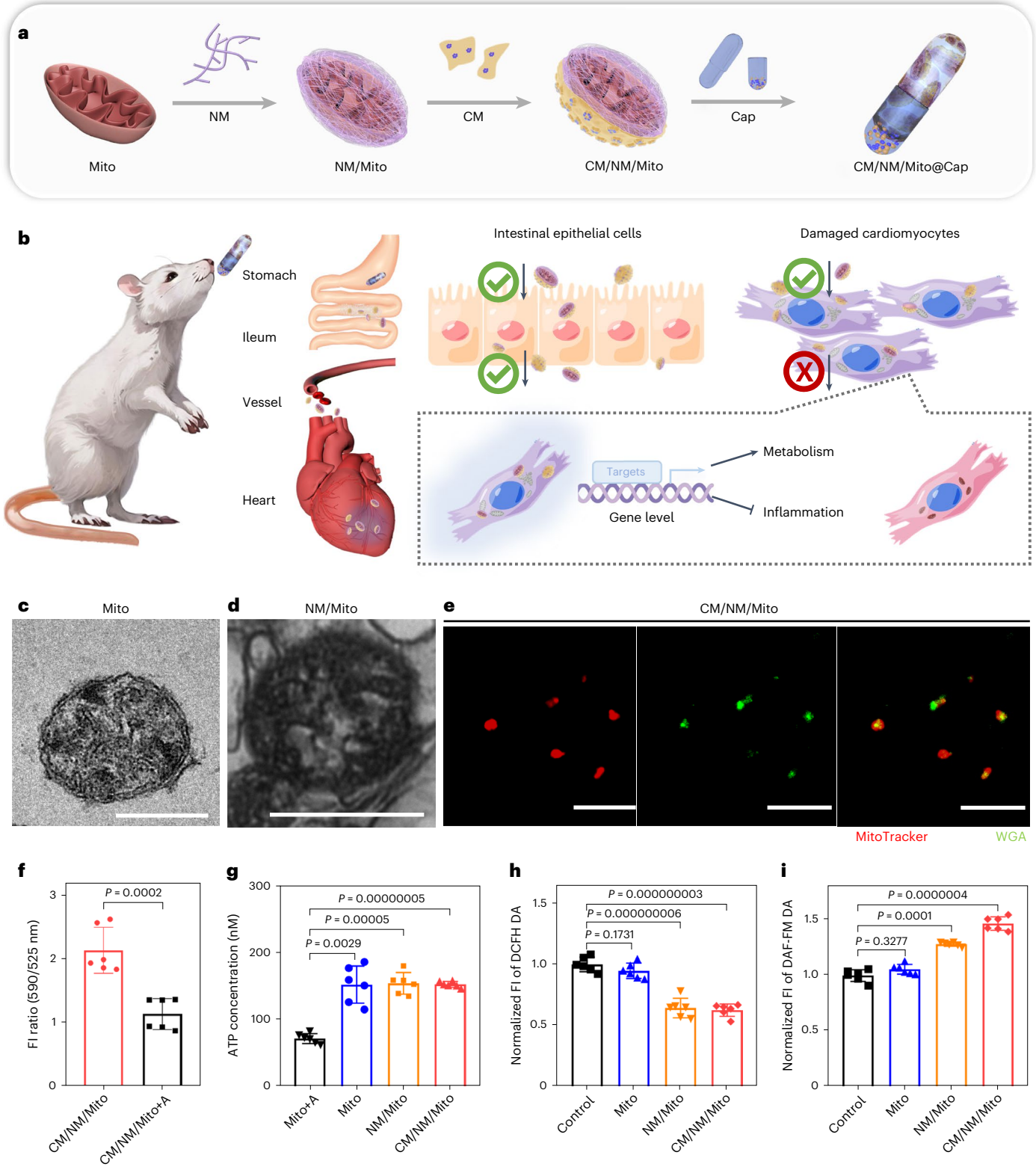

Fig. 1 | Schematic illustrations and characterization of CM/NM/Mito and the workflow of the oral delivery system CM/NM/Mito@Cap. a, The process of nanomotor and CM modification, and the compartmental design of the capsule. **b**, In vivo delivery and therapeutic pathway of CM/NM/Mito@Cap. **c**,**d**, TEM images of unmodified mitochondria (**c**) and NM/Mito (**d**). Scale bars, 500 nm. **e**, CLSM images of CM/NM/Mito. MitoTracker, NM/Mito; WGA, CM. Scale bars, 10 μm. **f**, Quantitative analysis of CM/NM/Mito after staining with JC-1, using antimycin A-treated CM/NM/Mito as a control. $n = 6$ biologically independent samples. FI, fluorescence intensity. **g**, ATP synthesis capability of antimycin A-treated unmodified mitochondria, unmodified mitochondria, NM/Mito and CM/NM/Mito in the presence of the substrate malic acid, glutamic acid and ADP. $n = 6$ biologically independent samples. **h**,**i**, Flow cytometry quantification of ROS (**h**) and NO (**i**) levels in damaged H9c2 cells after coincubation with different samples for 24 h. $n = 6$ biologically independent cell samples; the gating strategies are provided in Extended Data Fig. 2h. Data are presented as mean ± s.d. Statistical significance was calculated via two-tailed unpaired Student's t-test in **f**, and one-way analysis of variance with two-tailed least-significant difference (LSD) multiple-comparisons test in **h** and two-tailed Dunnett T3 multiple-comparisons test in **g**,**i**.

promote recovery of energy metabolism function in damaged cardiomyocytes. Coincubation with CM/NM/Mito also restored the ATP supply in damaged cardiomyocytes (Extended Data Fig. 4e). Evaluation of Ca^{2+} transients in spontaneously beating primary cardiomyocytes showed that coincubating damaged cardiomyocytes with CM/NM/Mito restored their Ca^{2+} transients to levels similar to those of normal cardiomyocytes (Fig. 2m)[29].

Ability of CM/NM/Mito to cross physiological barriers

To protect the CM/NM/Mito from being destroyed by gastric acid in the oral process, we packaged them in enteric capsules[30], creating CM/NM/Mito@Cap (Fig. 3a). As shown in Extended Data Fig. 5a and Fig. 3b,c, the capsules effectively protect the CM/NM/Mito from degradation in a simulated environment mimicking the pH value of gastric acid and generate gas in the intestinal environment[31]. In an everted gut sac model[32], the capsules containing the power model promoted CM/NM/Mito translocation through the mucus barrier and entry into the mucosal tissue (Fig. 3d). These results were further confirmed in a transwell-based intestinal epithelial barrier model[33] (Extended Data Fig. 5b).

Next, we tested whether oral CM/NM/Mito could reach the bloodstream. Ex vivo organ imaging and tissue slice analysis of small intestine demonstrated that CM/NM/Mito derived from CM/NM/Mito@Cap reached the intestine and was absorbed by intestinal epithelial cells (Fig. 3e–g); little exogenous mitochondria (derived from Mito@Cap and NM/Mito@Cap) localized to intestinal epithelial cells. Because substances absorbed by intestinal epithelial cells are transported to the capillaries and converge in the mesenteric vasculature[34], we also observed significant fluorescence of CM/NM/Mito in the mesenteric microvessels (Fig. 3h and Supplementary Fig. 5), which was also confirmed by pharmacokinetic analysis (Extended Data Fig. 5c).

Finally, we evaluated the ability of oral CM/NM/Mito to target the ischaemic heart. Acute IHD (for example, IRI) is characterized by high levels of ROS production and inflammation[35]. For rats with acute IHD that received CM/NM/Mito@Cap, CM/NM/Mito fluorescence in the damaged heart increased over time (Extended Data Fig. 5d,e and Fig. 3i). The percentage oral dose per gram of heart tissue for CM/NM/Mito was about 7.9% at 6 h after oral administration of CM/NM/Mito@Cap (Fig. 3j), while for exogenous mitochondria reached the heart in rats that received Mito@Cap and NM/Mito@Cap, it was only 1.0% and 1.1%, respectively. These results were also confirmed in a rat model of chronic IHD (that is, myocardial ischaemia) (Extended Data Fig. 5d,f and Fig. 3k,l). At 12 h, the percentage oral dose per gram of heart tissue in the CM/NM/Mito@Cap group was 2.9 and 2.7 times greater than that in the Mito@Cap and the NM/Mito@Cap groups, respectively. In addition, the delivery efficiency of CM/NM/Mito to the damaged heart when administered orally was 35.5% of that achieved via intravenous administration (Supplementary Fig. 6a). Moreover, the CM/Mito (without NM component, that is, without chemotactic ability) had poor cardiac penetration and retention with a cardiac delivery efficiency of 1.7% oral dose per gram of heart tissue. Different dosing frequencies of CM/NM/Mito@Cap may also have an impact on cardiac delivery efficiency (Extended Data Fig. 5g). Furthermore, CM/NM/Mito were also detected in the liver and kidney (Supplementary Fig. 6b). At the heart tissue level, the CM/NM/Mito were mainly concentrated in the distal left anterior descending artery (that is, the injured myocardium) (Extended Data Fig. 5h). At the cellular lever, CM/NM/Mito were effectively retained by damaged cardiomyocytes (Supplementary Fig. 7a–c). By contrast, CM/Mito delivered by CM/Mito@Cap had limited penetration in myocardial tissue and mostly accumulated in blood vessels (Supplementary Fig. 7d).

In vivo therapeutic effects and multi-omics analysis

In vivo, CM/NM/Mito exhibit good short-term biocompatibility (Supplementary Fig. 8). Rats with acute IHD were randomly divided into an intravenous CM/NM/Mito group and oral CM/NM/Mito@Cap or BB groups (Fig. 4a). Analysis of cardiac function and histopathological assessment suggest that intravenous administration of CM/NM/Mito rapidly conferred potent cardioprotection, and that oral administration of CM/NM/Mito@Cap can achieve efficacy comparable to that of the intravenous injection group by increasing the frequency and total dose of CM/NM/Mito@Cap (Fig. 4b–g and Supplementary Fig. 9). The selectivity of the administration routes makes it possible to apply CM/NM/Mito to the long-term treatment of chronic IHD.

To evaluate the therapeutic effect of CM/NM/Mito on chronic IHD (Fig. 4h), we induced myocardial ischaemia in rats, which decreased the ejection fraction of each experimental group to a level similar to that of the control group (Fig. 4i). Echocardiography indicated that although the CM/NM/Mito@Cap (5 times) group and the CM/NM/Mito intravenous (5 times) group were dosed equally, the ejection fraction of the former was maintained at around 75.3%, and that of the latter was 66.2%, indicating that intravenous administration was able to provide better recovery of cardiac function. However, similar therapeutic effects to intravenous administration could be achieved by increasing the oral dose: CM/NM/Mito@Cap (14 times) was able to restore the ejection fraction to about 76.5%. For the groups with similar dosage, in the first week, the ejection fraction of the CM/NM/Mito@Cap (15 times) group is better than that of the CM/NM/Mito@Cap (14 times) group (75.9% versus 71.6%). However, after the second week, there was little difference in the ejection fraction between the CM/NM/Mito@Cap (15 times) and CM/NM/ Mito@Cap (14 times) groups. In addition, both CM/NM/Mito@Cap (14 times) and CM/NM/Mito@Cap low (14 times) whose total oral dose was one-tenth of the former, provided better therapeutic effects than BB. There was no significant decrease in ejection fraction after discontinuing the medication as observed in the BB group (from 69.3% to 62.8%). In terms of pathological changes, rats that received oral administration of CM/NM/Mito@Cap (15 times) and CM/NM/Mito@Cap (14 times) exhibited the lowest fibrosis levels and the highest vessel density in the heart compared with other groups (Fig. 4j–l). Furthermore, CM/NM/Mito intracardiac injection restored mitochondrial function better than unmodified mitochondria (Supplementary Fig. 10), which may be due to the fact that the former not only has mitochondria with integrative structure, but also has the function of inflammatory microenvironment regulation. Taken together, these results suggest that oral administration of CM/NM/Mito@Cap could provide convenient, non-invasive, long-term

Fig. 2 | Cellular uptake, selective exocytosis and therapeutic effects of CM/NM/Mito. a, Schematic illustration of CM/NM/Mito establishing GJCs with recipient cells. **b**, CLSM images of normal IEC-6 and H9c2 cells forming GJCs with CM/NM/Mito in calcein medium. Black circles, calcein-stained area. Scale bars, 20 μm. **c**–**f**, CLSM images and quantification of different samples in normal IEC-6 (**c**,**d**) and H9c2 cells (**e**,**f**). MitoTracker, samples; DiO or WGA, membranes; Hoechst 33342, nuclei. Scale bars, 50 μm. (1) Unmodified mitochondria; (2) NM/Mito; (3) CM/NM/Mito. $n = 6$ biologically independent cell samples. **g**, The mechanism of selective exocytosis of CM/NM/Mito by cells with different states. **h**,**i**, The curve of Ca^{2+} levels in normal and damaged IEC-6 (**h**) and H9c2 cells (**i**). **j**,**k**, Quantification of CM/NM/Mito leakage ratio in normal and damaged IEC-6 (**j**) and H9c2 (**k**) cells. $n = 6$ biologically independent cell samples. **l**, CLSM images and Pearson's correlation coefficients showing the co-localization of the cells' own mitochondria with different samples in damaged H9c2 cells. MitoTracker Deep Red, samples; MitoTracker Green, cells' own mitochondria; Hoechst 33342, nucleus. Scale bars, 50 μm. **m**, Calcium transient of primary cardiomyocytes coincubated with different samples for 24 h. Data are presented as mean ± s.d. Statistical significance was calculated via one-way ANOVA with two-tailed LSD multiple-comparisons test in **d**,**f**, and two-tailed unpaired Student's *t*-test in **j**,**k**.

https://doi.org/10.1038/s41565-024-01681-7

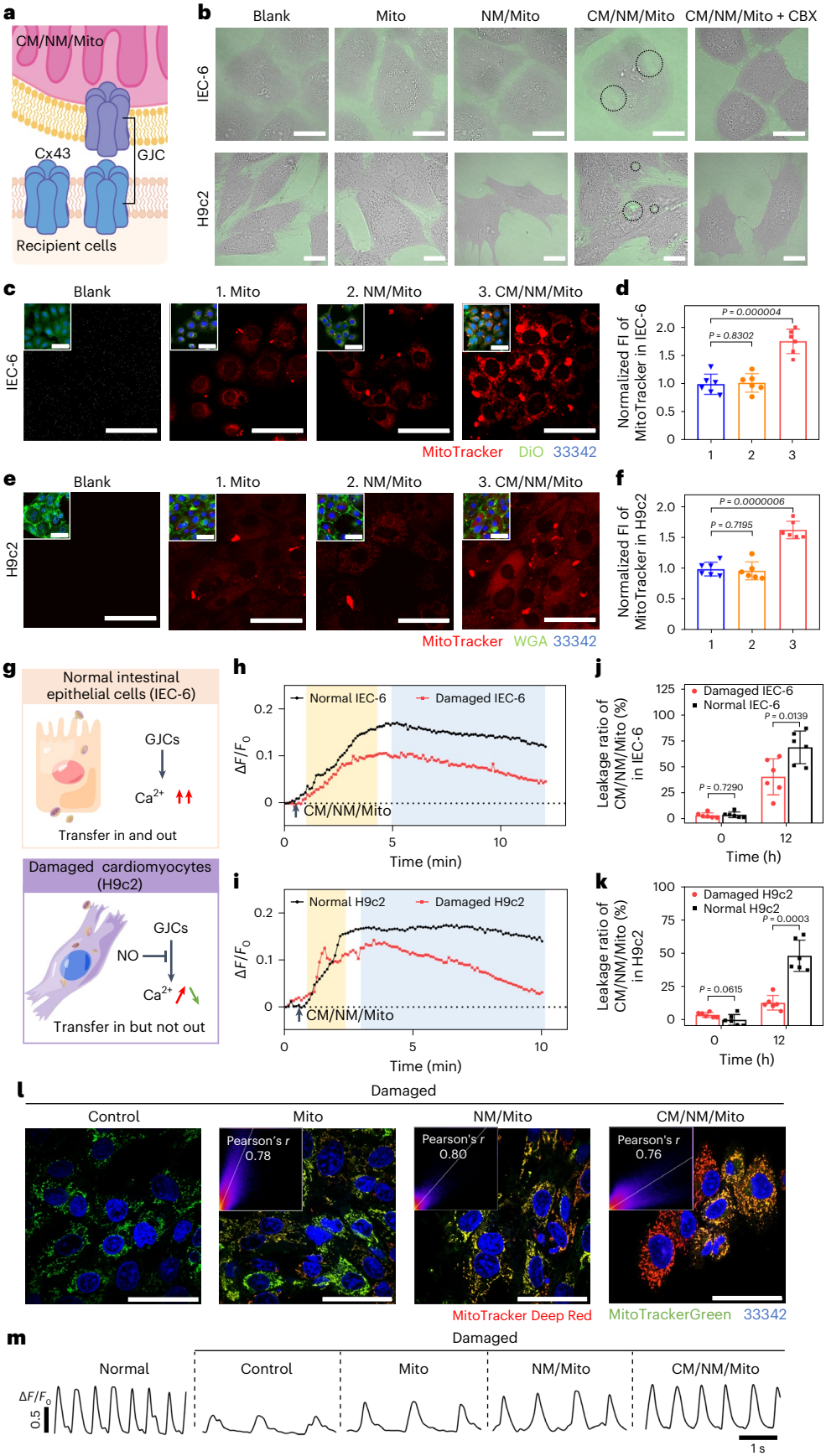

https://doi.org/10.1038/s41565-024-01681-7

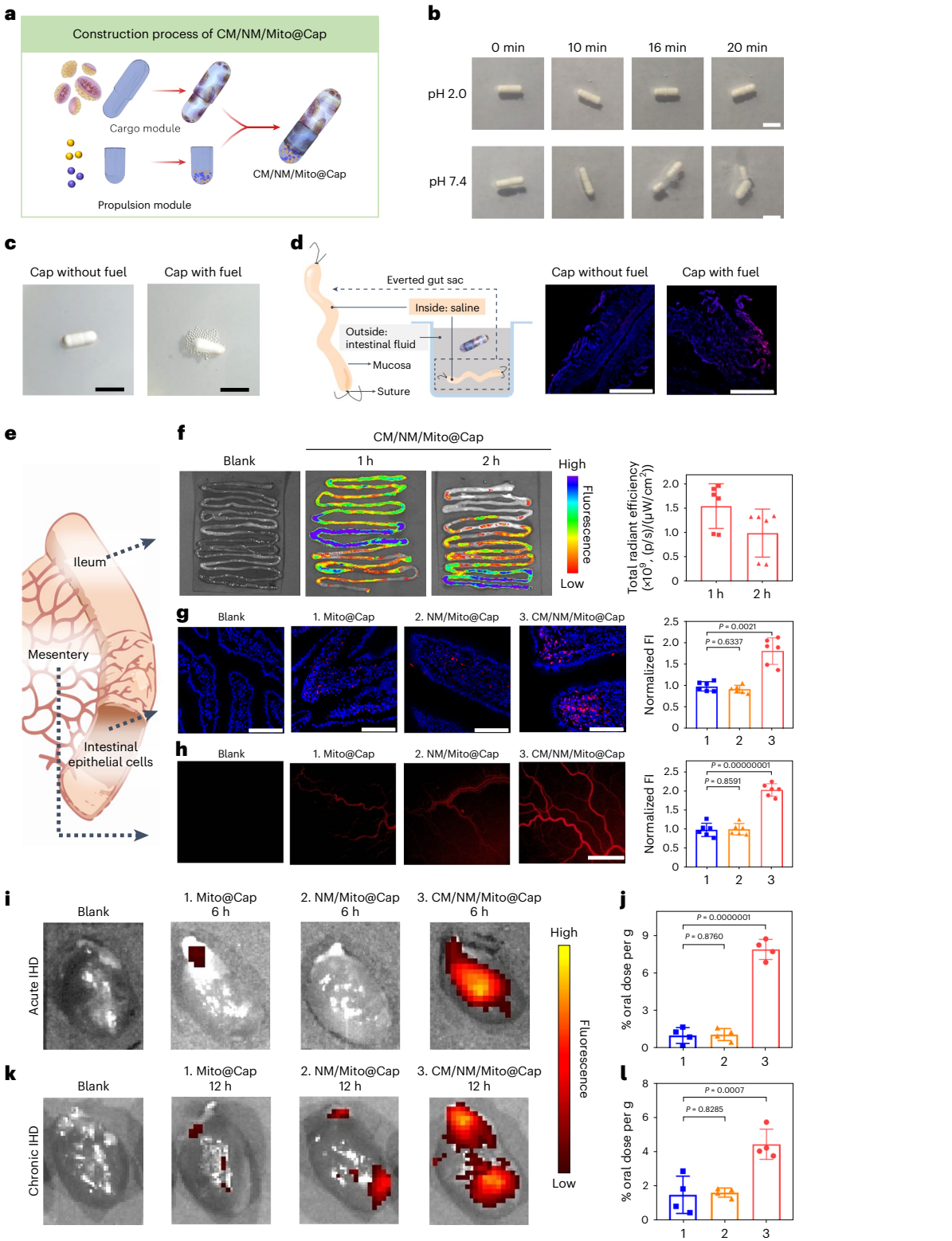

Fig. 3 | Characterization of CM/NM/Mito crossing multiple physiological barriers and targeting the ischaemic heart. a, Schematic illustration of the assembly process of CM/NM/Mito@Cap. **b**, Disintegration process of capsules with fuel in PBS. Scale bars, 5 mm. **c**, Gas production of capsules with or without fuel in the rat intestinal fluid. Scale bar, 5 mm. **d**. Schematic illustration of everted gut sac and CLSM images of ileal sections. MitoTracker, CM/NM/Mito; DAPI, nuclei. Scale bars, 500 μm. **e**, Schematic illustration of the observation site. **f**, Ex vivo imaging and quantification of intestinal tissues after oral administration of CM/NM/Mito@Cap in rats. $n = 6$ biologically independent animal samples. **g**,**h**, CLSM images and quantification of ileal sections (**g**), and in vivo fluorescence images and quantification of mesenteric microvasculature (**h**) after oral administration of (1) Mito@Cap, (2) NM/Mito@Cap and (3) CM/NM/Mito@Cap in rats. MitoTracker, samples; DAPI, nuclei. Scale bars, 100 μm. $n = 6$ biologically independent animal samples. **i**–**l**, Ex vivo imaging of hearts and cardiac delivery efficiency of (1) Mito@Cap, (2) NM/Mito@Cap and (3) CM/NM/Mito@Cap after oral administration in the acute IHD model (**i**,**j**) and in the chronic IHD model (**k**,**l**). $n = 4$ biologically independent animal samples. Data are presented as mean ± s.d. Statistical significance was calculated via one-way ANOVA with two-tailed Dunnett T3 multiple-comparisons test in **g** and two-tailed LSD multiple-comparisons test in **h**,**j**,**l**.

https://doi.org/10.1038/s41565-024-01681-7

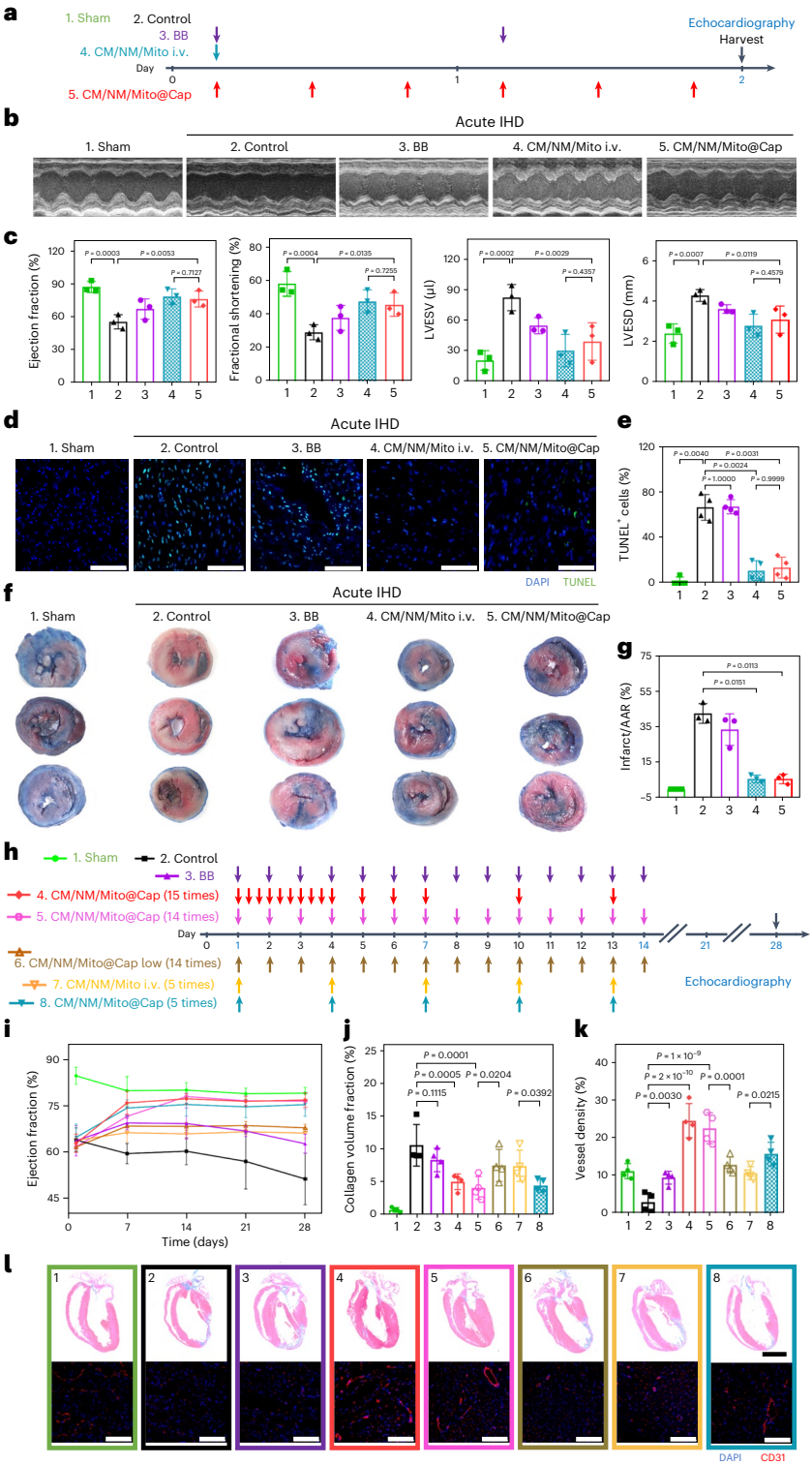

Fig. 4 | In vivo therapeutic efficacy of CM/NM/Mito@Cap on IHD. a, Schematic illustration of the animal treatment protocol in the acute IHD model. **b**,**c**, M-mode echocardiograms (**b**) and quantification (**c**) of cardiac function in acute IHD rats. $n = 3$ biologically independent animal samples. **d**,**e**, CLSM images (**d**) and quantification (**e**) of TUNEL-stained cardiac sections in the acute IHD rats. TUNEL, apoptotic cardiomyocytes; DAPI, nuclei. Scale bar, 100 μm. $n = 4$ biologically independent animal samples. **f**,**g**, Representative images (**f**) and quantification (**g**) of Evans blue/TTC-stained cardiac sections in the acute IHD rats. $n = 3$ biologically independent animal samples. Samples in **c**–**g**: (1) sham, (2) control, (3) oral administration of BB, (4) intravenous administration of CM/NM/Mito, (5) oral administration of CM/NM/Mito@Cap. **h**, Schematic illustration of the animal treatment protocol in the chronic IHD model. **i**, Curve of ejection fraction during the treatment in the chronic IHD model. $n = 3$ biologically independent animal samples in the sham, control, BB, CM/NM/Mito@Cap (15 times) and CM/NM/Mito intravenous (5 times) groups. $n = 5$ biologically independent animal samples in the CM/NM/Mito@Cap (14 times), CM/NM/Mito@Cap low (14 times) and CM/NM/Mito@Cap (5 times) groups. **j**,**k**, Quantification of collagen volume fraction (**j**) and vessel density (**k**) in the chronic IHD model. $n = 4$ biologically independent animal samples. **l**, Images of Masson-stained cardiac sections (scale bar, 5 mm) and CLSM images and of CD31-immunostained cardiac sections in the chronic IHD rats. CD31, vessels; DAPI, nuclei. Scale bars, 100 μm. Data are presented as mean ± s.d. Statistical significance was calculated via one-way ANOVA with two-tailed LSD multiple-comparisons test in **c**,**j**,**k** and two-tailed Dunnett T3 multiple-comparisons test in **e**,**g**.

https://doi.org/10.1038/s41565-024-01681-7

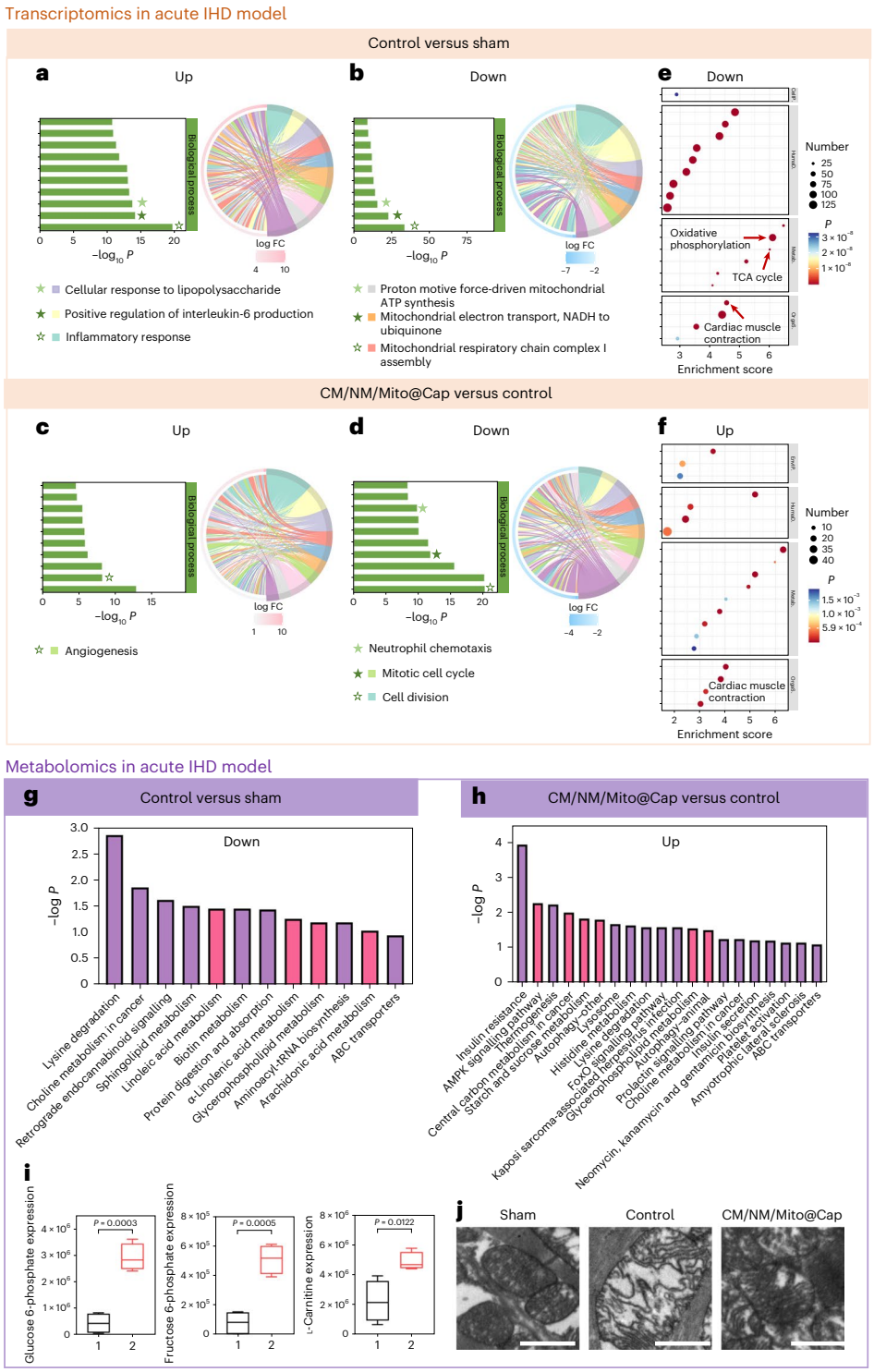

Fig. 5 | Cardiac multi-omics analysis of the CM/NM/Mito@Cap effect on acute IHD. a–**f**, Transcriptomics analysis in the acute IHD model. GO enrichment analysis showing DEGs in the control group compared with the sham group (**a**,**b**), DEGs in the CM/NM/Mito@Cap group compared with the control group (**c**,**d**) and corresponding KEGG pathway enrichment analysis (**e**,**f**). Histogram: top ten significantly enriched biological processes. The horizontal axis represents $-\log_{10} P$ of the pathway and the vertical axis represents the GO terms. Chord diagram: top ten significantly enriched GO terms, in which the right semicircle represents the names of ten GO terms, the left semicircle are DEGs in GO terms. The colour map represents the fold-change of genes ($\log_2$ scale), and the coloured bands connect a gene to a specific GO term. Bubble diagram: the top 20 significantly enriched KEGG terms. The horizontal axis represents the enrichment score, the vertical axis represents description and bubble sizes represent enriched gene counts. CellP., cellular processes; HumaD., human diseases; Metab., metabolism; OrgaS., organismal systems; EnvIP., environmental information processing. **g**–**i**, No-target metabolomic analysis in the acute IHD model: histograms of metabolic pathway enrichment analysis (**g**,**h**), and boxplots showing median (line in box), interquartile range (box), 1.5× interquartile range (whiskers), minima and maxima of representative differential metabolites, including glucose 6-phosphate, fructose 6-phosphate and L-carnitine (**i**) ((1) control; (2) oral administration of CM/NM/Mito@Cap). **j**, Cardiac TEM images showing mitochondria. Scale bar, 1 μm. In **a**–**i**, $n = 3$ biologically independent animal samples in the sham group, and $n = 4$ biologically independent animal samples in the control group and the oral administration of CM/NM/Mito@Cap group. In **a**–**f**, the P values were determined using the negative binomial distribution, and then the Benjamini–Hochberg procedure was used for multiple hypothesis testing correction. In **g**–**i**, statistical significance was calculated via a two-tailed unpaired Student's t-test.

https://doi.org/10.1038/s41565-024-01681-7

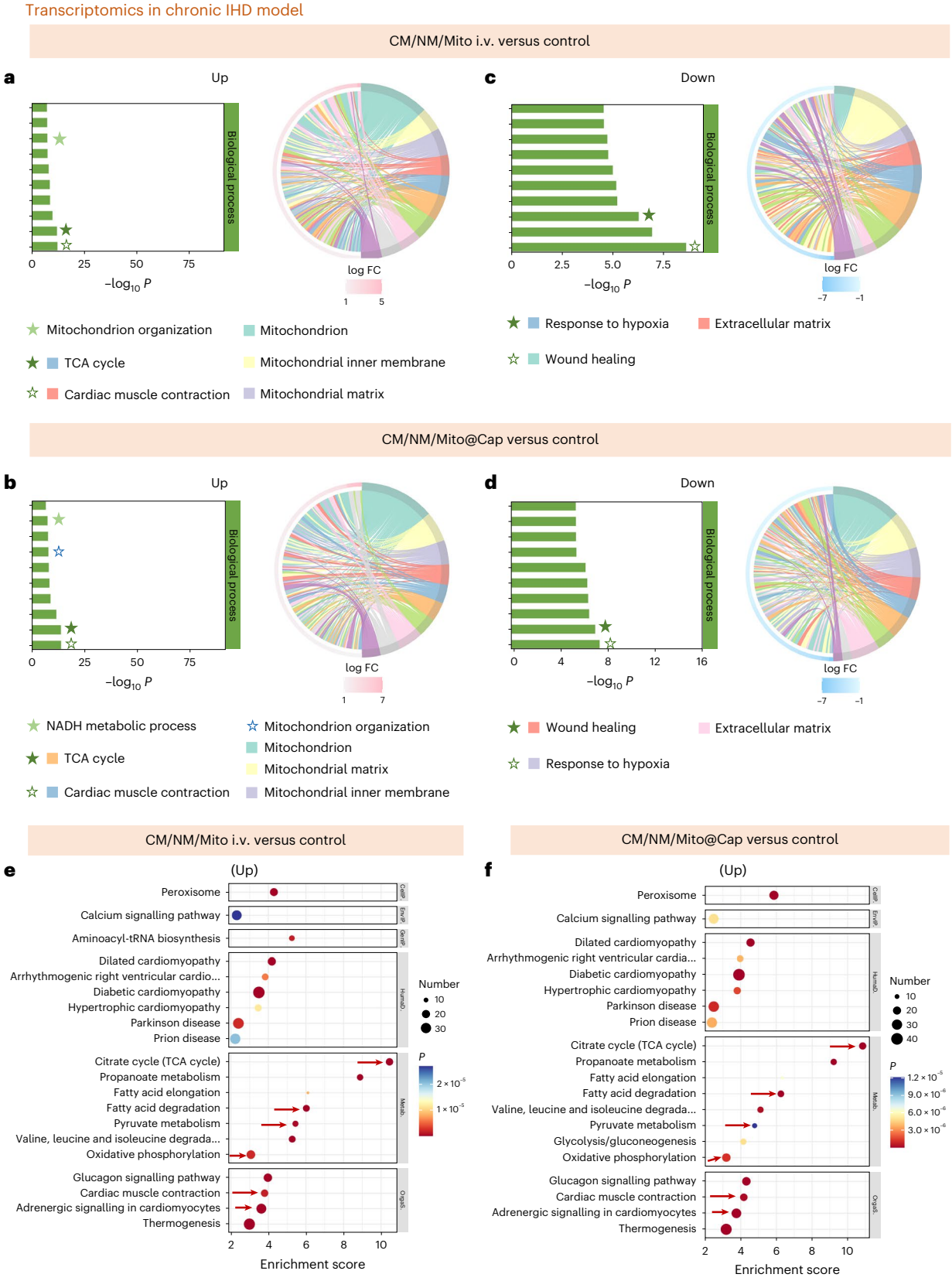

cardioprotection in the context of chronic IHD. In addition, the results in Extended Data Fig. 6 demonstrated the good biocompatibility of CM/NM/Mito@Cap in the long term.

We carried out transcriptome sequencing of heart tissue from rats with acute IHD treated with CM/NM/Mito@Cap or left untreated (Extended Data Fig. 7a). Gene Ontology (GO)-based functional enrichment analysis showed that treatment with CM/NM/Mito@Cap was associated with up-regulation of key genes involved in angiogenesis. In addition, the expression of genes associated with neutrophil chemotaxis was reduced in the CM/NM/Mito@Cap group compared with the untreated group, implying a reduction in cardiac inflammation (Fig. 5a–d and Supplementary Figs. 11 and 12). Mitochondrial

Fig. 6 | Cardiac transcriptomics analysis of the CM/NM/Mito@Cap effect on chronic IHD. a–**d**, GO enrichment analysis showing DEGs in the CM/NM/Mito intravenous group (**a**,**c**) and in the CM/NM/Mito@Cap group (**b**,**d**) compared with the control group. Histogram: top ten significantly enriched biological processes. The horizontal axis represents the $-\log_{10}(P)$ of the pathway and the vertical axis represents the GO terms. Chord diagram: top ten significantly enriched GO terms, in which the right semicircle represents the names of ten GO terms, and the left semicircle are DEGs in GO terms. The colour map represents the fold-change of genes ($\log_2$ scale), and the coloured bands connect a gene to a specific GO term. **e**,**f**, Bubble diagram showing the top 20 significantly enriched KEGG terms. The horizontal axis represents enrichment score, the vertical axis represents description and bubble sizes are represented as enriched gene counts. CellP., cellular processes; EnvIP., environmental information processing; GenIP., genetic information processing; HumaD., human diseases; Metab., metabolism; OrgaS., organismal systems. $n = 3$ biologically independent animal samples in per group. The P values were determined using the negative binomial distribution, and then the Benjamini–Hochberg procedure was used for multiple-hypothesis testing correction.

transplantation also affects the cardiomyocyte cell cycle[36]. Kyoto Encyclopedia of Genes and Genomes (KEGG) pathway enrichment analysis showed that multiple pathways beneficial for therapeutic efficacy, such as cardiac muscle contraction, were up-regulated in the CM/NM/Mito@Cap compared with the untreated group (Fig. 5e,f and Supplementary Figs. 13 and 14). To determine whether the changes observed at the transcript level affected downstream metabolites, we performed non-targeted metabolomics analysis. Overall, the metabolomics analysis showed that acute IHD disrupted cardiomyocyte lipid metabolism in a rat model, and that CM/NM/Mito@Cap treatment, in addition to rescuing cellular lipid metabolism, also comprehensively mobilized cellular energy metabolism and glucose metabolism to improve cellular metabolic function as a whole (Fig. 5g–i). Furthermore, transmission electron microscopy (TEM) analysis of the rat heart showed reduced mitochondrial swelling, disruption and cristae loss in cardiomyocytes after CM/NM/Mito@Cap treatment (Fig. 5j).

Next, we performed transcriptome sequencing of heart tissue from a rat model of chronic IHD (Extended Data Fig. 7b and Supplementary Figs. 15 and 16). Compared to the untreated group, genes that were significantly up-regulated after intravenous CM/NM/Mito or oral CM/NM/Mito@Cap treatment were associated with mitochondrial structure and function (Fig. 6a,b). In addition, genes related to the tricarboxylic acid cycle and cardiac muscle contraction were up-regulated in the heart after treatment. Genes that were down-regulated in the heart after treatment were mainly involved in biological processes related to the response to hypoxia, wound healing and especially the extracellular matrix (Fig. 6c,d). Moreover, KEGG pathway enrichment analysis (Fig. 6e,f) showed that the differentially expressed genes (DEGs) that were up-regulated in the oral CM/NM/Mito@Cap group compared with the untreated group were involved in cardiac muscle contraction and a variety of cellular metabolic processes, including energy metabolism and lipid metabolism. In addition, beneficial adrenergic signalling in cardiomyocytes was enhanced in rats treated with oral CM/NM/Mito@Cap or intravenous CM/NM/Mito[37]. The results of the multi-omics analysis were also validated by quantitative real-time polymerase chain reaction (qRT-PCR) (Supplementary Fig. 17). Taken together, oral administration of CM/NM/Mito@Cap exerts its therapeutic effects on chronic IHD by comprehensively rebuilding cardiac energy metabolism and attenuating myocardial fibrosis at the transcriptional level.

Conclusions

We synthesized nanomotorized mitochondria and validated their utility in mediating mitochondrial transplantation via oral administration to treat IHD. Modification of the nanomotors not only effectively maintained mitochondrial activity during the delivery process, but also enabled them to navigate to the damaged heart tissue via chemotaxis toward high levels of iNOS/ROS expression. In particular, the nanomotorized mitochondria quickly crossed the intestinal barrier and were effectively retained by damaged cardiomyocytes by regulating the intracellular Ca^{2+} levels with different states. The cardiac targeting efficiency of nanomotorized mitochondria packaged in enteric capsules and ingested orally can be increased from 1% (unmodified mitochondria) to 7.9% (percentage oral dose per gram of heart tissue). Oral administration of nanomotorized mitochondria not only significantly restored cardiac function in a rat model of IHD, but also maintained cardiac function at this level for 2 weeks after discontinuation. Furthermore, transcriptomic and metabolomic analyses showed that oral administration of CM/NM/Mito@Cap fully restored cardiomyocyte mitochondrial function in both acute and chronic IHD models, improving overall cellular lipid, glucose and energy metabolism, and significantly enhancing the contractile capacity of the cardiomyocytes. This non-invasive mitochondrial transplantation strategy has important implications for halting, rather than simply delaying, deterioration in patients with chronic IHD who require long-term medication.

Online content

Any methods, additional references, Nature Portfolio reporting summaries, source data, extended data, supplementary information, acknowledgements, peer review information; details of author contributions and competing interests; and statements of data and code availability are available at https://doi.org/10.1038/s41565-024-01681-7.

References

1. Brown, D. A. et al. Mitochondrial function as a therapeutic target in heart failure. *Nat. Rev. Cardiol.* **14**, 238–250 (2017).
2. Godoy, L. C. et al. Association of beta-blocker therapy with cardiovascular outcomes in patients with stable ischemic heart disease. *J. Am. Coll. Cardiol.* **81**, 2299–2311 (2023).
3. Cohn, P. F., Fox, K. M. & Daly, C. Silent myocardial ischemia. *Circulation* **108**, 1263–1277 (2003).
4. Ibanez, B. et al. 2017 ESC Guidelines for the management of acute myocardial infarction in patients presenting with ST-segment elevation: the Task Force for the management of acute myocardial infarction in patients presenting with ST-segment elevation of the European Society of Cardiology (ESC). *Eur. Heart J.* **39**, 119–177 (2018).
5. Ikeda, G. et al. Mitochondria-rich extracellular vesicles from autologous stem cell-derived cardiomyocytes restore energetics of ischemic myocardium. *J. Am. Coll. Cardiol.* **77**, 1073–1088 (2021).
6. Sun, M. et al. Mitochondrial transplantation as a novel therapeutic strategy for cardiovascular diseases. *J. Transl. Med.* **21**, 347 (2023).
7. Bertero, E., Maack, C. & O'Rourke, B. Mitochondrial transplantation in humans: 'magical' cure or cause for concern? *J. Clin. Invest.* **128**, 5191–5194 (2018).
8. Lightowlers, R. N., Chrzanowska-Lightowlers, Z. M. & Russell, O. M. Mitochondrial transplantation—a possible therapeutic for mitochondrial dysfunction? Mitochondrial transfer is a potential cure for many diseases but proof of efficacy and safety is still lacking. *EMBO Rep.* **21**, e50964 (2020).
9. Zhang, T. & Miao, C. Mitochondrial transplantation as a promising therapy for mitochondrial diseases. *Acta Pharm. Sin. B* **13**, 1028–1035 (2023).
10. McCully, J. D. et al. Injection of isolated mitochondria during early reperfusion for cardioprotection. *Am. J. Physiol. Heart Circ. Physiol.* **296**, H94–H105 (2009).
11. Sun, X. et al. Alda-1 treatment promotes the therapeutic effect of mitochondrial transplantation for myocardial ischemia-reperfusion injury. *Bioact. Mater.* **6**, 2058–2069 (2021).

12. Hayashida, K. et al. Exogenous mitochondrial transplantation improves survival and neurological outcomes after resuscitation from cardiac arrest. *BMC Med.* **21**, 56 (2023).
13. Baryakova, T. H., Pogostin, B. H., Langer, R. & McHugh, K. J. Overcoming barriers to patient adherence: the case for developing innovative drug delivery systems. *Nat. Rev. Drug Discov.* **22**, 387–409 (2023).
14. Chen, W., Huang, T., Shi, K., Chu, B. & Qian, Z. Chemotaxis-based self-accumulation of surface-engineered mitochondria for cancer therapeutic improvement. *Nano Today* **35**, 100966 (2020).
15. Chen, H. et al. A nitric-oxide driven chemotactic nanomotor for enhanced immunotherapy of glioblastoma. *Nat. Commun.* **14**, 941 (2023).
16. Tang, S. et al. Enzyme-powered Janus platelet cell robots for active and targeted drug delivery. *Sci. Robot.* **5**, eaba6137 (2020).
17. Lanza, I. R. & Nair, K. S. Functional assessment of isolated mitochondria in vitro. *Methods Enzymol.* **457**, 349–372 (2009).
18. Heitzer, T., Schlinzig, T., Krohn, K., Meinertz, T. & Münzel, T. Endothelial dysfunction, oxidative stress, and risk of cardiovascular events in patients with coronary artery disease. *Circulation* **104**, 2673–2678 (2001).
19. Li, T. et al. A universal chemotactic targeted delivery strategy for inflammatory diseases. *Adv. Mater.* **34**, e2206654 (2022).
20. Somasundar, A. et al. Positive and negative chemotaxis of enzyme-coated liposome motors. *Nat. Nanotechnol.* **14**, 1129–1134 (2019).
21. Michela, P., Velia, V., Aldo, P. & Ada, P. Role of connexin 43 in cardiovascular diseases. *Eur. J. Pharmacol.* **768**, 71–76 (2015).
22. Bennett, B. C. et al. An electrostatic mechanism for Ca^{2+}-mediated regulation of gap junction channels. *Nat. Commun.* **7**, 8770 (2016).
23. Islam, M. N. et al. Mitochondrial transfer from bone-marrow-derived stromal cells to pulmonary alveoli protects against acute lung injury. *Nat. Med.* **18**, 759–765 (2012).
24. Gadok, A. K. et al. Connectosomes for direct molecular delivery to the cellular cytoplasm. *J. Am. Chem. Soc.* **138**, 12833–12840 (2016).
25. Chen, P. et al. A plant-derived natural photosynthetic system for improving cell anabolism. *Nature* **612**, 546–554 (2022).
26. Huang, T. et al. Iron oxide nanoparticles augment the intercellular mitochondrial transfer-mediated therapy. *Sci. Adv.* **7**, eabj0534 (2021).
27. Massion, P. B., Feron, O., Dessy, C. & Balligand, J.-L. Nitric oxide and cardiac function: ten years after, and continuing. *Circ. Res.* **93**, 388–398 (2003).
28. Manders, E. M. M., Verbeek, F. J. & Aten, J. A. Measurement of co-localization of objects in dual-colour confocal images. *J. Microsc.* **169**, 375–382 (1993).
29. Zhu, P. et al. Ripk3 promotes ER stress-induced necroptosis in cardiac IR injury: a mechanism involving calcium overload/XO/ROS/mPTP pathway. *Redox Biol.* **16**, 157–168 (2018).
30. Han, X. et al. Zwitterionic micelles efficiently deliver oral insulin without opening tight junctions. *Nat. Nanotechnol.* **15**, 605–614 (2020).
31. Zhou, Y. et al. A pH-triggered self-unpacking capsule containing zwitterionic hydrogel-coated MOF nanoparticles for efficient oral exendin-4 delivery. *Adv. Mater.* **33**, e2102044 (2021).
32. Zhu, W. et al. Oral delivery of therapeutic antibodies with a transmucosal polymeric carrier. *ACS Nano* **17**, 4373–4386 (2023).
33. Pearce, S. C. et al. Intestinal in vitro and ex vivo models to study host–microbiome interactions and acute stressors. *Front. Physiol.* **9**, 1584 (2018).
34. Drucker, D. J. Advances in oral peptide therapeutics. *Nat. Rev. Drug Discov.* **19**, 277–289 (2020).
35. Yellon, D. M. & Hausenloy, D. J. Myocardial reperfusion injury. *N. Engl. J. Med.* **357**, 1121–1135 (2007).
36. Zhang, A. et al. Delivery of mitochondria confers cardioprotection through mitochondria replenishment and metabolic compliance. *Mol. Ther.* **31**, 1468–1479 (2023).
37. Tevaearai, H. T., Walton, G. B., Eckhart, A. D., Keys, J. R. & Koch, W. J. Donor heart contractile dysfunction following prolonged ex vivo preservation can be prevented by gene-mediated β-adrenergic signaling modulation. *Eur. J. Cardiothorac. Surg.* **22**, 733–737 (2002).

Methods

Cell culture

The H9c2 rat cardiomyocyte cell line (catalogue number XY-R025) and the IEC-6 rat intestinal epithelial cell line (catalogue number XY-R008) were purchased from Shanghai Xinyu Biological Technology. The huMSCs were provided by Nanjing Taisheng Biotechnology. Unless otherwise specified, H9c2 cells were cultured in Dulbecco's modified Eagle medium (DMEM, Sperikon Life Science & Biotechnology, catalogue number SP03010500) supplemented with 10% fetal bovine serum (FBS) and 1% penicillin/streptomycin in a humidified atmosphere that contained 5% CO_2 at 37 °C. The IEC-6 cells were cultured in complete medium containing insulin (0.1 U ml^{-1}). The huMSCs were cultured in complete medium containing 89% DMEM/F12, 10% FBS and 1% penicillin/streptomycin. All cell lines tested negative for mycoplasma contamination.

Animals

Experiments were performed on male SD rats (180 g body weight, 6–8 weeks, purchased from Spearfish (Beijing) Biotechnology). Rats were kept in a breeding colony with 12 h light/dark cycles in standard cages housing maximally five adult rats with ad libitum access to food and water. All animal experimental operations were in accordance with the specifications of the Guide for the Care and Use of Laboratory Animals, and all experimental procedures and protocols were approved by the Animal Experimentation Ethics Committee of Nanjing Normal University (approval number IACUC-20200802).

M-Arg synthesis

M-Arg was obtained by reacting L-arginine with methacrylic anhydride[15]. L-Arginine (11.5 mmol, Shanghai Yuanye Bio-Technology) was completely dissolved in a combination of deionized water (20 ml) and 1,4-dioxane (8.5 ml, Sinopharm Chemical Reagent). While stirring, triethylamine (32.3 mmol, Aladdin Chemistry) was introduced, and the solution was cooled using an ice/water bath. Methacrylic anhydride (18.9 mmol, Aladdin Chemistry) was added dropwise to the solution within 10 min, and the solution was then cooled to 0 °C. Next, the solution was removed from the ice/water bath and stirred at room temperature overnight. Then, the solution was slowly dripped into acetone (Sinopharm Chemical Reagent), and the lower precipitate was aspirated, centrifuged and washed with acetone. Finally, the precipitate was vacuum-dried to obtain M-Arg.

Diselenide cross-linker synthesis

To obtain the diselenide cross-linker[15], selenocysteamine hydrochloride (3.0 mmol, Shanghai Bide Pharmaceutical Technology) was dissolved in anhydrous dichloromethane (60.0 ml, J&K Scientific), and triethylamine (25.8 mmol) was added with stirring. The reaction was carried out for 30 min in an ice/water bath. Next, methacryloyl chloride (12.4 mmol, Sinopharm Chemical Reagent) was added dropwise to the solution, which was then removed from the ice/water batch and allowed to react at room temperature for 24 h in a nitrogen atmosphere. Impurities in the reaction solution were removed by extraction with deionized water. Subsequently, the solution was dried with anhydrous Na_2SO_4 (Sinopharm Chemical Reagent) overnight, and then the organic phase was removed by evaporation under reduced pressure. The product was purified on a silica gel column using a mixture of ethylacetate/petroleum ether (1/2, v/v) and subjected to rotary evaporation and drying to yield the ROS-responsive diselenide cross-linker.

Triphenylphosphine-NH_2 synthesis

To obtain triphenylphosphine (TPP)-NH_2 (ref. 38), a mixture of acetonitrile (40 ml), 2-bromoethylamine hydrobromide (10 mmol) and TPP (10 mmol) was condensed and refluxed at 90 °C for 24 h. After evaporation at 80 °C, the crystals were dissolved in distilled water. The pH of the solution was then adjusted to 11.0 with NaOH (2 M). After removing the amine with methanol and removing NaBr by filtering, ether precipitation was performed to yield TPP-NH_2.

CM preparation

CM was harvested as described in a previous publication, with minor changes[39]. Briefly, H9c2 cells were washed with PBS. After centrifugation at 800*g*, the cells were suspended in hypotonic lysing buffer containing Tris–HCl (30 mM), D-mannitol (225 mM), sucrose (75 mM), ethylene glycol tetraacetic acid (EGTA, 0.2 mM) and phenylmethanesulfonyl fluoride (PMSF, 1 mM) (all reagents were obtained from Shanghai Yuanye Bio-Technology). The cells were then disrupted using a Dounce homogenizer. After centrifugation at 20,000*g* for 25 min at 4 °C, the supernatant was collected and centrifuged again at 100,000*g* for 2 h at 4 °C. Then, the CM precipitate was resuspended in PBS containing PMSF and EGTA to a final total protein concentration of 500 μg ml^{-1}. To generate CM labelled with WGA, H9c2 cells were collected and stained with wheat germ agglutinin (WGA) (10 μg ml^{-1}, Beijing Solarbio Science & Technology, catalogue number I3300) for 30 min. After centrifugation to remove the staining solution, the cells were washed with PBS and centrifuged again to obtain the WGA-labelled H9c2 cells. Then, CM was prepared as described above.

Mitochondrial isolation

Mitochondria were isolated using a Mitochondrial Isolation Kit (Thermo Fisher Scientific, catalogue number 89874) according to the manufacturer's instructions[14,40]. Mitochondria obtained from 2×10^7 huMSCs were resuspended in 100 μl of PBS containing PMSF.

NM/Mito preparation

An unmodified mitochondrial suspension (1×10^{10} particles ml^{-1}, 100 μl) was mixed with *N*-acryloyloxysuccinimide aqueous solution (1 mg ml^{-1}, 100 μl), and the reaction was allowed to proceed for 6 h at 4 °C. After centrifugation at 12,000*g* for 5 min, 200 μl of PBS was added to induce dispersion, and mitochondria modified by the addition of carbon–carbon double bonds were obtained. Diselenide cross-linker (0.4 mg) and M-Arg (1.9 mg) were dissolved in 500 μl of PBS, and the resulting solution was mixed with 200 μl of mitochondria modified by the addition of carbon–carbon double bonds. *N*,*N*,*N*′,*N*′-Tetramethylethylenediamine (1.0 g ml^{-1}, 45 μl) and ammonium peroxodisulfate (1 g ml^{-1}, 25 μl) were added to the solution, and the reaction was allowed to proceed at 4 °C for 12 h in a nitrogen atmosphere. After centrifugation at 12,000*g* for 10 min at 4 °C, the NM/Mito precipitate was resuspended in PBS containing PMSF.

CM/NM/Mito and CM/Mito preparation

CM/NM/Mito and CM/Mito were obtained by electrostatic interaction between CM and NM/Mito or unmodified mitochondria[16]. First, an unmodified mitochondria suspension or an NM/Mito suspension (5×10^9 particles ml^{-1}, 200 μl) was added to polylysine-coated 24-well plate. The plate was centrifuged at 5,000*g* for 5 min to allow the unmodified mitochondria or NM/Mito to attach to the bottom of the wells, and the plates were incubated for 1 h. Then, the supernatant was removed, TPP-NH_2 (1 mg ml^{-1}, 200 μl) was added and the reaction was allowed to proceed for 0.5 h. After removal of the free TPP-NH_2, a CM suspension (protein concentration, 500 μg ml^{-1}, 200 μl) was added, and the reaction was allowed to proceed for 1 h. Next, the supernatant containing any unbound CM was removed, the wells were washed with PBS, and the CM/Mito or CM/NM/Mito were separated from the bottom of the plate by repeated pipetting and transferred to centrifuge tubes. After centrifugation at 12,000*g* for 5 min at 4 °C, the CM/Mtio or CM/NM/Mito precipitate was resuspended in PBS containing PMSF.

MitoTracker labelling

MitoTracker Deep Red FM (Cell Signaling Technology, catalogue number 8778) was added to suspended mitochondria, NM/Mito or CM/NM/Mito to reach the desired working concentration (in vitro

cellular uptake study, 1 μM; CM/NM/Mito cellular leakage ratio assay and Transwell-based intestinal barrier study, 50 μM; in vivo pharmacokinetic and targeting effect study, 100 μM), and the solution was incubated at room temperature in the dark for 30 min to allow the chloromethyl group of the probe to react with mitochondrial thiols.

Characterization of the physicochemical properties of the modified mitochondria

The surface morphology and dimensions of modified mitochondria were assessed using a JEM-2100 transmission electron microscope and a 200 kV field-emission transmission electron microscope (JEOL JEM-2100F). Zeta potential and particle size were measured using a Nano-Z Zetasizer (Malvern Instruments). The particles were counted via high-resolution, real-time dynamic nanoparticle detection using a NanoSight NS 300 apparatus (Malvern Instruments). The ^{1}H NMR spectra was recorded on a Bruker Avance 400 spectrometer.

NM/Mito protein detection by Coomassie brilliant blue staining

Mitochondria and NM/Mito were lysed with radio immunoprecipitation assay (RIPA) buffer to perform sodium dodecyl sulfate–polyacrylamide gel electrophoresis (SDS–PAGE). After electrophoresis, the gel was placed in Coomassie brilliant blue staining solution (Beyotime Biotechnology, catalogue number P0017B) and stained at room temperature for 1 h. After decolorization in a solution containing 40% ethanol, 10% acetic acid and 50% deionized water at room temperature for 6 h, the gels were imaged.

CM/NM/Mito protein detection by western blotting

Unmodified mitochondria, CM and CM/NM/Mito were lysed with RIPA buffer and subjected to SDS–PAGE. After electrophoresis, the proteins were transferred to polyvinylidene difluoride membranes. The membranes were then blocked with non-fat milk, followed by incubation with primary antibodies (anti-Cx43: Proteintech, catalogue number 26980-1-AP (1:1,000 dilution); anti-Na/K ATPase: Abcam, catalogue number ab76020 (1:20,000 dilution)) and then secondary antibodies, and the chemiluminescent signal was detected using an imaging system (Tanon 5200 Multi).

Mitochondrial membrane potential detection by JC-1 labelling

Unmodified mitochondria, NM/Mito and CM/NM/Mito were treated with antimycin A (1 mM) for 30 min to serve as negative controls. The negative controls, unmodified mitochondria, NM/Mito and CM/NM/Mito were then incubated with the JC-1 probe (20 μM, FcMACS, catalogue number FMS-FZ006) at room temperature for 15 min. After washing with PBS and centrifuging at 12,000*g* for 10 min, the samples labelled with JC-1 were resuspended in PBS. The fluorescence intensity (excitation/emission, 488 nm/525 nm and 488 nm/590 nm) was detected using a fluorescence spectrophotometer (Hitachi F4600).

CM/NM/Mito bioactivity detection by ATP synthesis assay

The assay solution was prepared on ice (all reagents were purchased from Sigma) and consisted of 15 μl of mixed substrate (10 mM glutamate and 5 mM malate), 15 μl of ADP (10 mM) and 20 μl of antimycin A-treated unmodified mitochondria, unmodified mitochondria, NM/Mito or CM/NM/Mito (1×10^9 particles ml^{-1}). Using an ATP assay kit (Beyotime Biotechnology, catalogue number S0026) according to the manufacturer's instructions, 100 μl of assay working solution and 50 μl of the assay solution described above were added to each well of a black 96-well plate, and the luminescence intensity was measured using a multifunctional enzyme labelling instrument (TECAN Spark).

CM/NM/Mito bioactivity detection by mitochondrial complex analysis

An Enhanced BCA Protein Assay Kit (Beyotime Biotechnology, catalogue number P0010S) was used to quantify the unmodified mitochondrial, NM/Mito and CM/NM/Mito samples. The activity of mitochondria complex I and mitochondria complex V was assessed by colorimetry using commercial kits (Abbkine, catalogue numbers KTB1850, KTB1890) with a multifunctional enzyme-labelling instrument according to the manufacturer's instructions.

Detection of cellular ROS and NO levels by flow cytometry

H9c2 cells were inoculated into six-well plates and incubated overnight. Then, normal cells or hypoxia reoxygenation (HR)-injured cells were coincubated with CM/NM/Mito (5×10^6 particles ml^{-1}) for another 24 h. An ROS fluorescent probe (DCFH-DA) and a NO fluorescent probe (DAF-FM DA) were diluted to 10 μM and 2.5 μM, respectively, and added to the cells, which were then incubated for 30 min at 37 °C according to the kit instructions (Beyotime Biotechnology, catalogue numbers S0033S, S0019). The stained cells were collected and immediately subjected to flow cytometry analysis using a BD Accuri C6 Plus flow cytometer. Here, the cells were subjected to HR injury as follows: the cells were washed several times with PBS, cultured in a glucose-free and serum-free DMEM, and incubated in an Anaeropack hypoxia box (Mitsubishi Gas Chemical, 0.1% O_2 and 5% CO_2) for 3 h, followed by reoxygenation in the complete medium containing glucose and 10% FBS in a 21% O_2 and 5% CO_2 atmosphere.

Assessment of chemotaxis behaviour using a Y channel

A glass-bottomed Y channel was customized to have the following dimensions: the main channel was 1 cm long and 0.4 cm wide, and the branch channels were 1 cm long and 0.3 cm wide. To create a chemokine gradient, agarose gels (1%, w/v) containing lysates of normal H9c2 cells or damaged H9c2 cells (prestimulated for 24 h with 1 μg ml^{-1} lipopolysaccharides (LPS)) were prepared. As shown in Extended Data Fig. 3a, equivalent volumes (500 μl of the agarose gels contained 250 μl of cell lysates (1×10^6 cells ml^{-1})) were loaded into reservoirs ii (damaged) and iii (normal) of the branching channels, and the channels were filled with 400 μl of PBS. Then, 20 μl of MitoTracker-labelled unmodified mitochondria or CM/NM/Mito was gently dropped into reservoir i (samples). Fluorescence images of reservoirs ii and iii were taken with an inverted fluorescence microscope (MSHOT MF53-N) at specific time points, and the fluorescence intensity was analysed using Image J v.1.54f.

Assessment of chemotaxis behaviour using a Ψ microfluidic device

A glass-bottomed Ψ microfluidic device was customized to have the following dimensions: 2.2 cm long, 1.5 mm wide, 0.3 mm high. MitoTracker-labelled unmodified mitochondria or CM/NM/Mito (1×10^9 particles ml^{-1}) were injected into channel ii at a flow rate of 0.6 ml h^{-1}. Lysates of normal H9c2 cells and LPS-treated H9c2 cells (prestimulated for 24 h with 1 μg ml^{-1} LPS) were injected into channels i and iii at the same flow rate. Once the flow rate had stabilized, an inverted fluorescence microscope was used to continuously scan and record the outlet for 1 min (30 frames per second). The normalized fluorescence intensity perpendicular to the flow direction was measured using Image J v.1.54f.

Visualization of GJC formation by calcein staining

To carry out the calcein staining process[24], IEC-6 cells and H9c2 cells were inoculated into glass-bottomed confocal microscopy dishes and cultured overnight. After washing with PBS, the cells were incubated in conditioned medium containing calcein (50 nM, Beijing Solarbio Science & Technology, catalogue number C7600) and unmodified mitochondria, NM/Mito or CM/NM/Mito (5×10^6) for 30 min. Then, confocal laser scanning microscopy (CLSM) with an Olympus FV3000 was performed to observe the calcein-stained cells. A portion of the cells were incubated with carbenoxolone (CBX, 100 μM, Shanghai Yuanye Bio-Technology, catalogue number 5697-56-3) for 2 h before the addition of the CM/NM/Mito to block GJC formation.

Assessment of GJC formation by calcein release assay

IEC-6 cells and H9c2 cells were inoculated into 96-well plates and cultured overnight. After washing with PBS, the cells were incubated in conditioned medium containing calcein-AM (500 nM, Beyotime Biotechnology, catalogue number C2012) for 30 min. Subsequently, the cells were incubated in serum-free DMEM for 30 min to convert the intracellular calcein-AM to calcein, which only diffuses across the cell membrane at very low levels. After washing with PBS, the cells were incubated in 200 µl of serum-free DMEM containing unmodified mitochondria, NM/Mito or CM/NM/Mito (1×10^6) for 30 min. Calcein fluorescence in the supernatant was then detected using a multifunctional enzyme-labelling instrument to assess the level of calcein release from the cells. A portion of the cells was incubated with CBX (100 µM) for 2 h before the addition of CM/NM/Mito to block GJC formation.

Cellular uptake assessment

IEC-6 cells and H9c2 cells were inoculated into glass-bottomed confocal microscopy dishes and incubated overnight. The next day, the cells were coincubated with MitoTracker-labelled unmodified mitochondria, NM/Mito or CM/NM/Mito (5×10^6 particles ml^{-1}) for 6 h, and the IEC-6 and H9c2 cells were stained with 3,3'-dioctadecyloxacarbocyanine perchlorate (DiO) (5 µM, Beyotime Biotechnology, catalogue number C1038) and WGA (10 µg mL^{-1}), respectively. Cellular uptake results were observed by CLSM.

Intracellular Ca^{2+} imaging

IEC-6 cells and H9c2 cells were inoculated into glass-bottomed confocal microscopy dishes and cultured overnight. Cells were stimulated with LPS (1 µg ml^{-1}) for 24 h and then washed several times with PBS. The cells were then coincubated with the Fluo-4 AM probe (4 µM, Beyotime Biotechnology, catalogue number S1060) for 90 min, followed by incubation in serum-free DMEM for another 30 min, during which time the Fluo-4 AM taken up by the cells was converted to Fluo-4 and bound to intracellular Ca^{2+}. After washing the cells several times with PBS, a peristaltic pump (Baoding Chuangrui Precision Pump, CM1000) was used to inject buffer (10 mM HEPES, 136.0 mM NaCl, 4.8 mM KCl, 1.2 mM $CaCl_2$, 1.2 mM $MgSO_4$, 4.0 mM glucose and 0.1% BSA)[41] into the medium, and the baseline Ca^{2+} fluorescence (F_0) was recorded for 1 min using an orthogonal fluorescence microscope (Ningbo YONG XIN Optics, NE950). Subsequently, CM/NM/Mito (5×10^6 particles ml^{-1}) were injected into the medium, and the change in cellular Ca^{2+} fluorescence (ΔF) was recorded. Finally, the fluorescence intensity was analysed using Image J v.1.54f) and expressed as $\Delta F/F_0$.

CM/NM/Mito leakage assay

IEC-6 cells and H9c2 cells were inoculated into 12-well plates and cultured overnight. Normal ICE-6 cells and ICE-6 cells prestimulated with LPS (1 µg ml^{-1}) for 24 h, and normal H9c2 cells and HR-injured H9c2 cells, were coincubated with MitoTracker-labelled CM/NM/Mito (5×10^6 particles ml^{-1}) for 6 h. The culture supernatant was then removed and the cells were washed several times with PBS, followed by further incubation in fresh DMEM. At 0 h and 12 h, cell supernatants were collected, and the cells were lysed with RIPA buffer to obtain cell lysates. The MitoTracker fluorescence intensity in the culture supernatants and cell lysates was detected using a multifunctional enzyme marker. The CM/NM/Mito content in the culture supernatants and cell lysates was calculated by comparing the fluorescence intensity to a standard curve. Finally, the CM/NM/Mito leakage ratio was expressed as the ratio of the CM/NM/Mito content in the culture supernatant to the total CM/NM/Mito content (the sum of CM/NM/Mito content in the supernatant and cell lysate).

Characterization of membrane fusion of CM/NM/Mito with recipient cells

IEC-6 cells and H9c2 cells were inoculated into glass-bottomed confocal microscopy dishes, and the H9c2 cells were subjected to HR injury. Subsequently, the cells were coincubated with CM/NM/Mito (5×10^6 particles ml^{-1}) double-labelled with WGA and MitoTracker for 6 h. The recipient cell membranes were stained with DiL (5 µM, Jiangsu Keygen Biotech, catalogue number KGMP002), and the nuclei were stained with Hoechst 33342. The cells were then observed by CLSM and Pearson's r values were analysed using the Colco2 plugin for Image J v.1.54f.

Characterization of mitochondrial fusion between CM/NM/Mito and damaged cardiomyocytes

Endogenous HR-injured H9c2 cell mitochondria were labelled with MitoTracker Green (20 nM, Beyotime Biotechnology, catalogue number C1048). Subsequently, the cells were coincubated with MitoTracker Deep Red-labelled unmodified mitochondria, NM/Mito or CM/NM/Mito (5×10^6 particles ml^{-1}) for 6 h, and recipient cell nuclei were stained with Hoechst 33342. The cells were then observed by CLSM and analysed using Image J v.1.54f.

Measuring cardiomyocyte ATP content

H9c2 cells were inoculated into six-well plates and cultured overnight. HR-injured H9c2 cells were coincubated with unmodified mitochondria, NM/Mito or CM/NM/Mito (5×10^6 particles ml^{-1}). After washing several times with PBS, the cells were lysed with 200 µl lysis buffer from the ATP assay kit. The lysates were centrifuged at 12,000g for 5 min at 4 °C, and the supernatant was collected for testing. In total, 100 µl of assay working solution and 20 µl of lysates were added to each well of a black 96-well plate, and the luminescence intensity was measured using a multifunctional enzyme-labelling instrument.

Morphological analysis of cardiomyocyte mitochondria

H9c2 cells were inoculated into glass-bottomed confocal microscopy dishes and cultured overnight. HR-injured H9c2 cells were coincubated with unmodified mitochondria, NM/Mito or CM/NM/Mito (5×10^6 particles ml^{-1}). After washing several times with PBS, cells were fixed in 100% cold methanol for 15 min at −20 °C. CLSM images of the mitochondria were taken. A previously published Image J v.1.54f macro was used to quantify average mitochondrial roundness[42].

Ca^{2+} transient detection in primary cardiomyocytes

Neonatal rats (<24 h old) were purchased from Spearfish (Beijing) Biotechnology. Primary cardiomyocytes were isolated from the neonatal rats[43], resuspended in prewarmed complete medium containing 88.5% Iscove's modified Dulbecco's medium (IMDM), 10% FBS, 0.5% glutamine and 1% penicillin/streptomycin and inoculated into glass-bottomed confocal microscopy dishes precoated with fibronectin (25 µg ml^{-1} Beijing Solarbio Science & Technology, catalogue number F8180). After 48 h, the primary cardiomyocytes were transferred to glucose-free and serum-free IMDM and incubated in an Anaeropack hypoxia box for 1 h. The cells were then reoxygenated in complete medium in a 21% O_2 and 5% CO_2 atmosphere, and coincubated with unmodified mitochondria, NM/Mito or CM/NM/Mito (5×10^6 particles ml^{-1}). After incubation for 24 h, the cells were stained with Fluo-4 AM (4 µM) for 90 min. Intracellular calcium transients in the spontaneously beating primary cardiomyocytes were recorded by CLSM.

Assessment of CM/NM/Mito and endogenous mitochondria secretion in a transwell-based intestinal epithelial barrier model

IEC-6 cells were inoculated at 10^4 cells per well into the type I collagen-coated upper chamber (pore size, 3 µm) of a Transwell device and cultured for 18 days to form a tightly connected monolayer[33]. Then, 200 µl of unmodified mitochondria or CM/NM/Mito (5×10^7 particles ml^{-1}) with MitoTracker Deep Red labelling were added to the upper chamber, and 500 µl of complete medium was added to the lower chamber. The medium in the lower chamber was collected at

different time points and replaced with fresh complete medium. Fluorescence intensity in the medium was detected using a multifunctional enzyme-labelling instrument and summed to calculate the cumulative increase in fluorescence at each time point.

Preparation and characterization of the enteric capsules

To assess the pH responsiveness of the capsules, the cap section (propulsion module) of large commercial enteric capsules (2 cm long and 0.5 cm wide) was filled with sodium bicarbonate (60 mg) and citric acid (60 mg) and nested into a body section (cargo module) filled with Evans blue. The capsules were then immersed in PBS at pH 2.0 or 7.4, and their degradation was recorded. Similarly, compartmentalized enteric capsules were prepared using small customized enteric capsules (Yuyan Instruments, catalogue number YG01-2, 0.5 cm long and 0.2 cm wide) filled with sodium bicarbonate (6 mg) and citric acid (6 mg), and their degradation was recorded at the same pH values. In subsequent experiments, the cargo module of each capsule was filled with unmodified mitochondria, NM/Mito or CM/NM/Mito and nested with the propulsion module.

Characterization of enteric capsule degradation in intestinal fluid

To obtain the intestinal fluid, a sonde needle was inserted into the small intestine, and the intestinal contents were flushed with 20 ml of cold PBS[44]. The flushed intestinal contents were then centrifuged at 1,500*g* for 10 min to remove particulates, yielding supernatants comprising intestinal fluid. Capsules with or without sodium bicarbonate (6 mg) and citric acid (6 mg) were placed in the intestinal fluid, and their degradation was recorded.

Assessment of CM/NM/Mito@Cap transmucosal penetration in the everted gut sac model

Briefly, small-intestine segments were harvested from rats and gently flushed with saline. One end of the gut segment was ligated by suturing, the lumen was filled with saline and the other end of the gut sac was also ligated shut[32]. The filled sac was then placed in a dish containing 5 ml of intestinal fluid and CM/NM/Mito@Cap (containing 1×10^8 MitoTracker-labelled CM/NM/Mito) with or without sodium bicarbonate (6 mg) and citric acid (6 mg) for 1 h. The everted gut sac was then flash-frozen and sectioned, and CLSM images were taken.

Mesenteric microvascular imaging

Rats ingested one Mito@Cap, NM/Mito@Cap or CM/NM/Mito@Cap containing 1×10^9 MitoTracker-labelled particless and were anaesthetized 3 h later. An abdominal incision was made, and the mesenteric microvasculature was observed using a fluorescence inverted microscope.

In vivo pharmacokinetics assay

Rats ingested one Mito@Cap or CM/NM/Mito@Cap containing 1×10^9 MitoTracker-labelled unmodified mitochondria or CM/NM/Mito. Serum was collected at different time points after oral administration of the capsules. Fluorescence intensity in the serum was measured using a multifunctional enzyme marker.

In vivo biocompatibility assessment

Rats were injected with 1×10^9 CM/NM/Mito into the tail vein, or received oral administration of one CM/NM/Mito@Cap containing 1×10^9 CM/NM/Mito or 14 CM/NM/Mito@Cap containing 1×10^8 CM/NM/Mito. Then, 24 h or 28 days later, blood and major organs were collected for analysis. The organs were fixed in 4% paraformaldehyde for 48 h, dehydrated, clarified, embedded in paraffin, sectioned to perform haematoxylin and eosin and myeloperoxidase (MPO)-immunohistochemical (anti-MPO: Abcam, catalogue number ab208670 (1:1,000 dilution)) staining. The sections were then observed using a light microscope and analysed using Image J v.1.54f.

Establishment of rat models of IHD

To establish the rat model of acute IHD, that is, IRI, male SD rats weighing 180 g (6–8 weeks) were anaesthetized with isoflurane gas and mechanically ventilated using a ventilator (Beijing Zhishu Duobao Biological Technology, DB038X). Myocardial ischaemia was produced by ligating the distal third of the left anterior descending artery with a slipknot for 1 h, after which the slipknot was released to induce reperfusion. For the rat model of chronic IHD, that is, myocardial infarction, the left anterior descending artery was permanently ligated with a tight knot. In the sham group, the same surgery was performed, but a ligature was not applied.

Evaluation of CM/NM/Mito cardiac targeting efficiency and biodistribution in vivo

Rats with acute IHD received oral administration of one Mito@Cap, NM/Mito@Cap or CM/NM/Mito@Cap containing 1×10^9 MitoTracker-labelled particles. Rats with chronic IHD received oral administration of one Mito@Cap, NM/Mito@Cap, CM/Mito@Cap or CM/NM/Mito@Cap containing 1×10^8 MitoTracker-labelled particles. In addition, one group of rats with chronic IHD was injected with 1×10^8 CM/NM/Mito into the tail vein. One group of rats with chronic IHD received oral administration of one CM/NM/Mito@Cap containing 3×10^8 MitoTracker-labelled particles. One group of rats with chronic IHD received oral administration of three CM/NM/Mito@Cap containing 1×10^8 MitoTracker-labelled particles. The rat hearts were removed for imaging at different time points. Images were acquired and analysed using IVIS Lumina III, living image system 4.5.5 software. Rats with acute IHD that received oral administration of CM/NM/Mito@Cap were killed after 6 h, and their hearts were removed and sectioned at the proximal, middle and distal left anterior descending artery. After staining the nuclei with DAPI, CM/NM/Mito accumulation at different sites in the heart was assessed by CLSM imaging. Rats with chronic IHD that received oral administration of CM/Mito and CM/NM/Mito@Cap were killed after 12 h, and their hearts were removed and sectioned at the distal left anterior descending artery. After staining nuclei with DAPI, cardiomyocytes with cTnI (Abcam, catalogue number ab209809 (1:250 dilution)), endothelial cells with CD31 (Abcam, catalogue number ab281583 (1:500 dilution)) and smooth muscle cells or fibroblasts with α-smooth muscle actin (Cell Signaling Technology, catalogue number 19245 (1:500 dilution)), CM/NM/Mito accumulation in different cells was assessed by CLSM imaging.

In addition, rat hearts, livers, spleens, lungs and kidneys were collected and weighed. The tissues were then lysed with RIPA buffer at a ratio of 1 ml buffer to 100 mg tissue, and homogenized using a tissue grinder. The homogenized tissue was centrifuged at 1,500*g* for 10 min, the supernatant was collected, and the fluorescence intensity in the supernatant was measured using a multifunctional enzyme marker. The number of modified mitochondria in each tissue was calculated by comparing the fluorescence intensity to a standard curve. The percentage oral dose and injected dose rate (% oral dose and % ID) were then calculated using the following formulas: % oral dose = (number of modified mitochondria in organ/total number of orally administered modified mitochondria) × 100%; % ID = (number of modified mitochondria in organ/total number of injected modified mitochondria) × 100%. Oral dose percentage per g was expressed as the ratio of oral dose percentage to organ mass.

Animal groups and treatment protocols for the in vivo therapeutic effect experiments

Rats with acute IHD were randomly divided into the following five groups: a sham group, a control group, a BB group, a CM/NM/Mito intravenous group and a CM/NM/Mito@Cap group. Rats in the control group did not receive any treatment. Rats in the BB group were treated by gavage with BB (25 mg per kg (body weight)) every day after reperfusion. Rats in the CM/NM/Mito intravenous group were

injected with 1×10^9 CM/NM/Mito once after reperfusion. Rats in the CM/NM/Mito@Cap group received oral administration of CM/NM/Mito@Cap containing 1×10^9 CM/NM/Mito three times a day for two consecutive days. At the end of treatment, rats were killed with isoflurane for tissue harvest.

Rats with chronic IHD were randomly divided into the following eight groups: a sham group, a control group, a BB group, a CM/NM/Mito@Cap (15 times) group, a CM/NM/Mito@Cap (14 times) group, a CM/NM/Mito@Cap low (14 times) group, a CM/NM/Mito@Cap (5 times) group and a CM/NM/Mito intravenous (5 times) group. Rats in the control group did not receive any treatment. For rats in the BB group, BB (25 mg per kg (body weight)) was administered orally every day for two consecutive weeks. For rats in the CM/NM/Mito@Cap (15 times) group, CM/NM/Mito@Cap containing 1×10^8 CM/NM/Mito was administered orally three times a day for the first 3 days, once a day from the fourth day to the seventh day, and every 3 days from the eighth to the fourteenth day after surgery. For rats in the CM/NM/Mito@Cap (14 times) group, CM/NM/Mito@Cap containing 1×10^8 CM/NM/Mito was administered orally every day for two consecutive weeks. For rats in the CM/NM/Mito@Cap low (14 times) group, CM/NM/Mito@Cap containing 1×10^7 CM/NM/Mito was administered orally every day for two consecutive weeks. For rats in the CM/NM/Mito@Cap low (5 times) group, CM/NM/Mito@Cap containing 1×10^8 CM/NM/Mito was administered orally on the first, fourth, seventh, tenth and thirteenth day after surgery. For rats in the CM/NM/Mito i.v. (5 times) group, 1×10^8 CM/NM/Mito were injected on the first, fourth, seventh, tenth and thirteenth day after surgery. At the end of treatment, rats were killed with isoflurane for tissue harvest.

Echocardiography analysis of cardiac function

To assess cardiac function, rats were anaesthetized with isoflurane, and M-mode images were acquired and analysed using a high-frequency high-resolution ultrasound system (VisualSonics, Vevo2100). For rats with acute IHD, cardiac function was measured after 48 h of reperfusion. For rats with chronic IHD, cardiac function was measured every week.

TUNEL assay for detection of cardiomyocyte apoptosis in vivo

Frozen heart tissue sections were stained using a one-step terminal deoxynucleotidyl transferase dUTP nick end labeling (TUNEL) apoptosis assay kit (Beyotime Biotechnology, catalogue number C1088) to detect apoptotic cells. After staining the nuclei with DAPI, the cells were imaged by CLSM.

Assessment of infarction area by Evans blue/TTC staining

After 48 h of reperfusion, rats were anaesthetized with pentobarbital, and 0.25% Evans blue (Beijing Solarbio Science & Technology, catalogue number E8010) was injected into the right auricle of the heart. Then, the heart was quickly excised, rinsed with saline and immediately frozen at −80 °C for 15 min. The frozen heart was quickly sliced into four to five sections and incubated in 2% TTC (Beijing Solarbio Science & Technology, catalogue number G3005) at 37 °C for 30 min. The sections were fixed with 4% paraformaldehyde. The stained areas in each section were quantified using Image J v.1.54f. The area at risk included both the red ischaemic area and the white myocardial infarction areas. The infarction size was expressed as the percentage of total tissue defined as the area at risk.

Assessment of cardiac repair by Masson staining and CD31 immunostaining

Rat hearts were harvested, sliced into 5 µm sections, and stained with Masson's Trichrome Stain Kit (Beijing Solarbio Science & Technology, catalogue number G1340). The arterioles were identified with CD31 to quantify vessel density using an automated function (VesselJ) of Image J v.1.54f[45].

Bioactivity detection of fused mitochondria by mitochondrial complex analysis and ATP synthesis assay

Rats with chronic IHD were randomly divided into the following three groups: a control group, an unmodified mitochondria group and a CM/NM/Mito group. Rats in the control group did not receive any treatment. For rats in the other two groups, 5×10^6 unmodified mitochondria or CM/NM/Mito were administered via intramyocardial injection after surgery. Seven days later, rat hearts were harvested. After isolating the fused mitochondria from heart tissue, the activity of mitochondria complex I and mitochondria complex V was assessed by colorimetry using commercial kits with a multifunctional enzyme-labelling instrument following the manufacturer's instructions. An ATP synthesis assay was performed in the assay solution containing 15 µl of mixed substrate (10 mM glutamate and 5 mM malate), 15 µl of ADP (10 mM) and equal volumes of fused mitochondria isolated from the control group, the unmodified mitochondria group and the CM/NM/Mito group.

Transcriptomics analysis

Heart tissue from each treatment group in acute IHD rats (sham group, $n = 3$; control group, $n = 4$; oral administration of CM/NM/Mito@Cap group, $n = 4$) and chronic IHD rats (control group, $n = 3$; oral administration of CM/NM/Mito@Cap group, $n = 3$; intravenous administration of CM/NM/Mito (once) group, $n = 3$) was collected, and total RNA was extracted. The RNA purity was evaluated using a NanoDrop 2000/c spectrophotometer (Thermo Scientific), and libraries were constructed using a VAHTS Universal V6 RNA-seq Library Prep Kit. The transcriptome sequencing and analysis were conducted by OE Biotech. The libraries were sequenced on a Lumina Novaseq 6000 platform, and 150 bp paired-end reads were generated. HISAT was used to map the clean reads to the reference genome. Fragments per kilobase per million of each gene was calculated, and the read count for each gene was obtained using HTSeq-count. Then, principal component analysis was performed using R v.3.2.0. DEGs between two treatment groups were defined as having a q-value <0.05 and fold-change >2 or <0.5. The hypergeometric distribution of the DEGs was confirmed, and R v.3.2.0 was used to perform GO and KEGG pathway enrichment analyses and generate the relevant figures. Bioinformatic analysis was performed using the OECloud tools at https://cloud.oebiotech.com/task/.

pRT-PCR

Heart tissue was collected, and total RNA was extracted and immediately stored at −80 °C. Complementary DNAs were synthesized using the HiScript Q RT SuperMix for qPCR with gDNA wiper (Vazyme, catalogue number R123) according to the manufacturer's instructions. pRT-PCR was performed on a QuantStudio 6 Flex Real-Time PCR System using ChamQ Universal SYBR qPCR master mix (Vazyme, catalogue number Q711-02). Gene expression levels were normalized to those of Actb. Primers used in this study are shown in Supplementary Table 1.

Metabolomics analysis

Heart tissue from each treatment group in the acute IHD rats (sham group, $n = 3$; control group, $n = 4$, oral administration of CM/NM/Mito@Cap group, $n = 4$) was collected. The tissues were ground and filtered for liquid chromatography–mass spectrometry analysis. Metabolic profiling data was acquired using an ACQUITY UPLC I-Class system (Waters) and a Q-Exactive quadrupole Orbitrap mass spectrometer equipped with a heated electrospray ionization source (Thermo Fisher Scientific). The raw data were processed using Progenesis QI v.2.3 software (Nonlinear Dynamics). After compound identification, the extracted data were used to generate a data matrix. Differentially expressed metabolites were defined as those with variable importance of projection values (obtained by orthogonal partial least-squares-discriminant analysis) greater than 1.0 and P values (obtained by two-tailed Student's t-test) less than 0.05.

Statistics and reproducibility

Differences between the two groups were analysed by a two-tailed unpaired Student's *t*-test. Differences among multiple groups were analysed using one-way analysis of variance (ANOVA) with two-tailed LSD or Dunnett T3 multiple-comparisons tests. All statistical analyses were performed on Excel v.2019, SPSS v.22.0 and GraphPad Prism v.8. Statistical tests and *P* values are detailed in the figure legends. The results for Figs. 1c–e, 2h,i,l,m and 3b,c and Extended Data Figs. 1a–c,i,j, 2b,c,h, 3g,h, 4b and 5a were obtained after at least three independent repetitions of the experiment. Data were combined from two independent experiments in Fig. 1f and Extended Data Figs. 2d,e and 4d. Data were obtained from one representative of three independent experiments in Figs. 1g–i, 2b–f,j,k, 3d,f–l, 4b and 5j and Extended Data Figs. 2f–g, 3b–e, 4a,e; 5b,d–h and 6c,e.

Reporting summary

Further information on research design is available in the Nature Portfolio Reporting Summary linked to this article.

Data availability

The main data supporting the results in this study are available within the paper and its Supplementary Information. There are no data from third-party or publicly available datasets. RNA sequencing data are deposited in NCBI's Sequence Read Archive (SRA) and are accessible through accession numbers PRJNA1089164 and PRJNA1089186. Raw data of non-targeted metabolomics analysis are deposited in MetaboLights and are accessible through accession number MTBLS9785. All data generated as part of this study are available from the corresponding author upon reasonable request. Source data for Figs. 1–5 are available in separate source data files for Figs. 1f–i, 2d,f,h–k,m, 3f–h,j,l, 4c,e,g,i–k and 5g–i, respectively. Source data for Extended Data Figs. 1–6 are available in separate source data files for Extended Data Figs. 1b,c, 2c,d–g, 3c,e,g,h, 4a,d,e and 5b,c,e–h; Extended Data Fig. 6a, b, d. Source data are provided with this paper.

References

38. Tang, X. et al. Lipophilic NO-driven nanomotors as drug balloon coating for the treatment of atherosclerosis. *Small* **19**, 2203238 (2023).
39. Zhang, Q. et al. Neutrophil membrane-coated nanoparticles inhibit synovial inflammation and alleviate joint damage in inflammatory arthritis. *Nat. Nanotechnol.* **13**, 1182–1190 (2018).
40. Chen, W., Shi, K., Chu, B., Wei, X. & Qian, Z. Mitochondrial surface engineering for multidrug resistance reversal. *Nano Lett.* **19**, 2905–2913 (2019).
41. Xie, C. et al. Irisin controls growth, intracellular Ca^{2+} signals, and mitochondrial thermogenesis in cardiomyoblasts. *PLoS One* **10**, e0136816 (2015).
42. Dagda, R. K. et al. Loss of PINK1 function promotes mitophagy through effects on oxidative stress and mitochondrial fission. *J. Biol. Chem.* **284**, 13843–13855 (2009).
43. Vandergriff, A. C., Hensley, M. T. & Cheng, K. Isolation and cryopreservation of neonatal rat cardiomyocytes. *J. Vis. Exp.* **9**, e52726 (2015).
44. Yamagata, T. et al. Characterization of insulin protection properties of complexation hydrogels in gastric and intestinal enzyme fluids. *J. Control. Release* **112**, 343–349 (2006).
45. Rabiolo, A., Bignami, F., Rama, P. & Ferrari, G. VesselJ: a new tool for semiautomatic measurement of corneal neovascularization. *Invest. Ophthalmol. Vis. Sci.* **56**, 8199–8206 (2015).
46. Masuzawa, A. et al. Transplantation of autologously derived mitochondria protects the heart from ischemia-reperfusion injury. *Am. J. Physiol. Heart Circ. Physiol.* **304**, H966–H982 (2013).
47. Cowan, D. B. et al. Intracoronary delivery of mitochondria to the ischemic heart for cardioprotection. *PLoS One* **11**, e0160889 (2016).
48. Kaza, A. K. et al. Myocardial rescue with autologous mitochondrial transplantation in a porcine model of ischemia/reperfusion. *J. Thorac. Cardiovasc. Surg.* **153**, 934–943 (2017).
49. Shin, B. et al. A novel biological strategy for myocardial protection by intracoronary delivery of mitochondria: safety and efficacy. *JACC Basic Transl. Sci.* **4**, 871–888 (2019).
50. Blitzer, D. et al. Delayed transplantation of autologous mitochondria for cardioprotection in a porcine model. *Ann. Thorac. Surg.* **109**, 711–719 (2020).
51. Guariento, A. et al. Mitochondrial transplantation for myocardial protection in ex-situ-perfused hearts donated after circulatory death. *J. Heart Lung Transplant.* **39**, 1279–1288 (2020).
52. Guariento, A. et al. Preischemic autologous mitochondrial transplantation by intracoronary injection for myocardial protection. *J. Thorac. Cardiovasc. Surg.* **160**, e15–e29 (2020).
53. Sun, X. et al. Intravenous transplantation of an ischemic-specific peptide-TPP-mitochondrial compound alleviates myocardial ischemic reperfusion injury. *ACS Nano* **17**, 896–909 (2023).
54. Emani, S. M., Piekarski, B. L., Harrild, D., Del Nido, P. J. & McCully, J. D. Autologous mitochondrial transplantation for dysfunction after ischemia-reperfusion injury. *J. Thorac. Cardiovasc. Surg.* **154**, 286–289 (2017).
55. Guariento, A. et al. Autologous mitochondrial transplantation for cardiogenic shock in pediatric patients following ischemia-reperfusion injury. *J. Thorac. Cardiovasc. Surg.* **162**, 992–1001 (2021).
56. Kristensen, K. L., Rauer, L. J., Mortensen, P. E. & Kjeldsen, B. J. Reoperation for bleeding in cardiac surgery. *Interact. Cardiovasc. Thorac. Surg.* **14**, 709–713 (2012).
57. Zubrzycki, M. et al. Assessment and pathophysiology of pain in cardiac surgery. *J. Pain. Res.* **11**, 1599–1611 (2018).
58. Tanner, T. G. & Colvin, M. O. Pulmonary complications of cardiac surgery. *Lung* **198**, 889–896 (2020).
59. Kubota, H. et al. Deep sternal wound infection after cardiac surgery. *J. Cardiothorac. Surg.* **8**, 132 (2013).
60. Doll, J. A. et al. Management of percutaneous coronary intervention complications: algorithms from the 2018 and 2019 Seattle percutaneous coronary intervention complications conference. *Circ. Cardiovasc. Interv.* **13**, e008962 (2020).
61. Stern, S. & Bayes de Luna, A. Coronary artery spasm: a 2009 update. *Circulation* **119**, 2531–2534 (2009).

Acknowledgements

This work was supported by the National Natural Science Foundation of China (22175096 (C.M.), 22275095 (M.W.), 82272098 (M.Z.)), the Priority Academic Program Development of Jiangsu Higher Education Institution, Jiangsu Key Laboratory of Biofunctional Materials and Jiangsu Collaborative Innovation Center of Biomedical Functional Materials. We thank L. Bianji for editing the English text of a draft of this manuscript.

Author contributions

J.S., C.M., M.Z. and M.W. conceived and designed the project. Z.W. and L.C. prepared the samples and conducted most of the measurements. W.G. helped with the synthesis of materials. W.J. performed the assessment of chemotactic behaviour. H.N., J.W. and J.L. assisted in animal experiments. Z.W. and M.W. wrote the manuscript. All authors discussed the results and commented on the manuscript.

Competing interests

The authors declare no competing interests.

Additional information

Extended data is available for this paper at https://doi.org/10.1038/s41565-024-01681-7.

Supplementary information The online version contains supplementary material available at https://doi.org/10.1038/s41565-024-01681-7.

Correspondence and requests for materials should be addressed to Chun Mao, Min Zhou or Mimi Wan.

Peer review information *Nature Nanotechnology* thanks Huile Gao, Catherine Gorick and Gokhan Burcin Kubat for their contribution to the peer review of this work.

https://doi.org/10.1038/s41565-024-01681-7

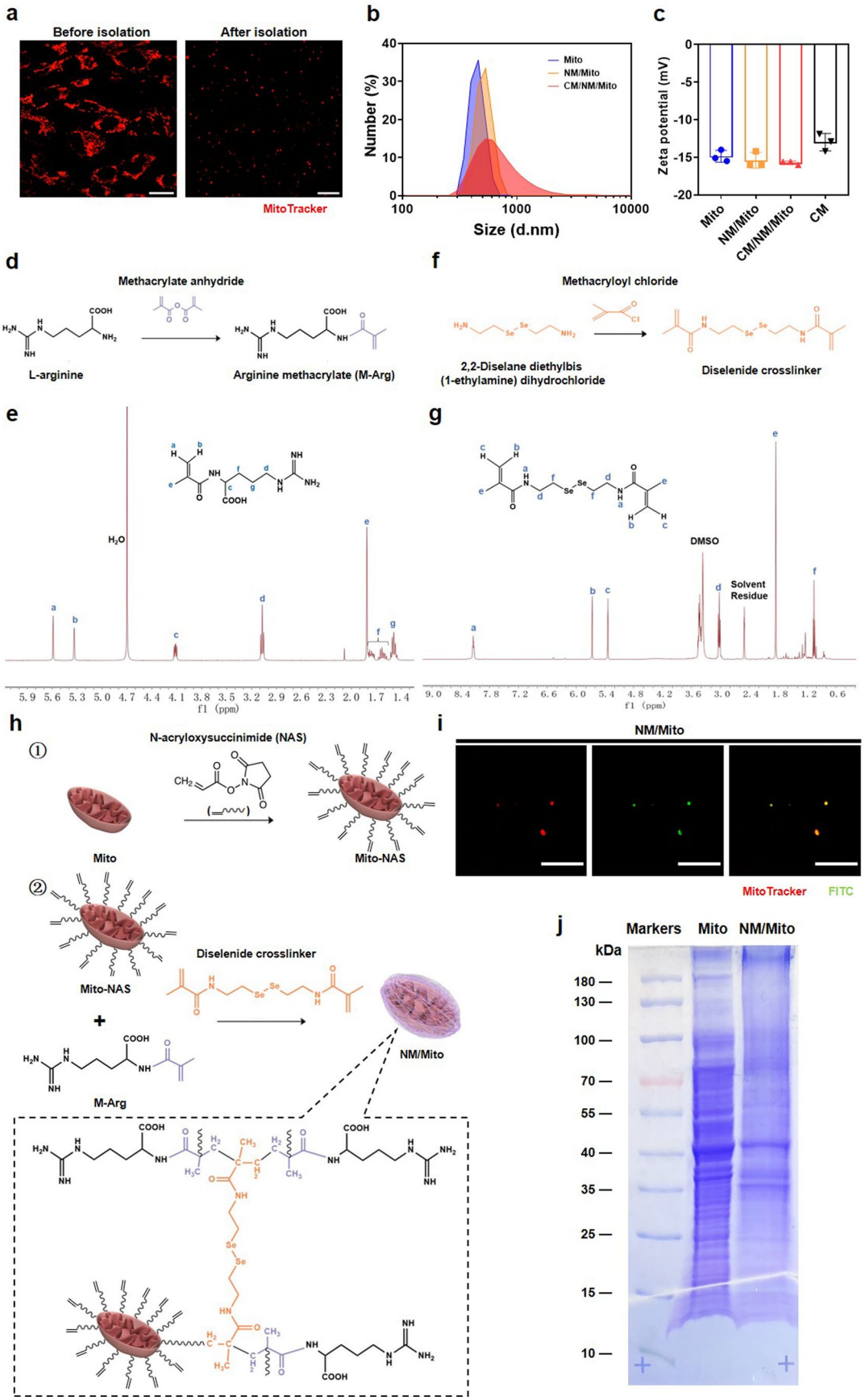

Extended Data Fig. 1 | See next page for caption.

https://doi.org/10.1038/s41565-024-01681-7

Extended Data Fig. 1 | Isolation and nanomotorization of mitochondria. **a**. CLSM images of MitoTracker Deep Red labelled huMSCs and their mitochondria before and after isolation (scale bar: 20 μm). **b** and **c**. The hydrated diameter and zeta potential of mitochondria, NM/Mito and CM/NM/Mito. Data are presented as means ± SD (n = 3 biologically independent samples). **d**. Synthesis process of M-Arg, the basic unit of NM. **e**. ^{1}H NMR of M-Arg in D_2O. **f**. Synthesis process of the diselenide cross-linker. **g**. ^{1}H NMR of diselenide cross-linker in DMSO-d6. **h**. Possible synthesis process of NM/Mito. **i**. CLSM images of NM/Mito. (NM was labelled with FITC, and mitochondria was labelled with MitoTracker Deep Red, scale bar: 10 μm). **j**. Coomassie brilliant blue staining of mitochondria and NM/Mito after SDS–PAGE.

https://doi.org/10.1038/s41565-024-01681-7

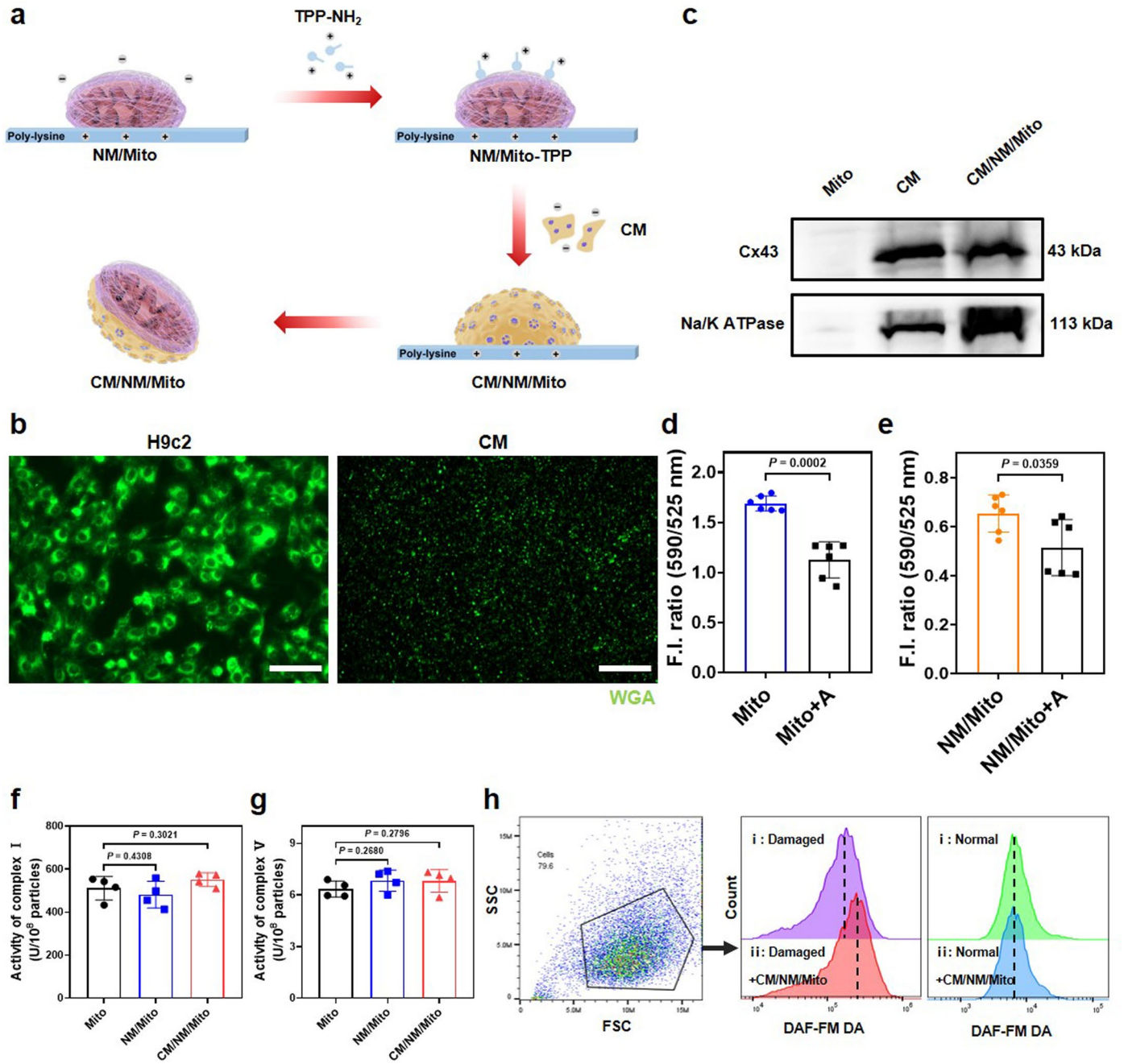

Extended Data Fig. 2 | Construction and characterization of CM/NM/Mito. **a**. Synthesis process of CM/NM/Mito. **b**. Fluorescence images of WGA-labelled H9c2 cells and CM before and after lysis (scale bar: 100 μm). **c**. Western blotting of cardiomyocyte membrane markers. Cx43: connexin-43, Na/K ATPase: sodium-potassium ATPase. **d** and **e**. Quantitative analysis of unmodified mitochondria and NM/Mito after staining with JC-1, using antimycin A-treated unmodified mitochondria and NM/Mito as the control (n = 6 biologically independent samples). **f** and **g**. Mitochondrial complexes I (**f**) and V (**g**) analysis of unmodified mitochondria, NM/Mito and CM/NM/Mito (n = 4 biologically independent samples). **h**. Flow cytometric analysis of cellular NO levels of normal and damaged H9c2 cells after incubation with CM/NM/Mito for 24 h. The gating strategies were corresponded to Fig. 1h and i. Data were presented as means ± SD. Statistical significance was calculated via two-tailed unpaired Student's t test in **d**, **e**, and one-way ANOVA with two-tailed LSD multiple comparisons test in **f**, **g**. Source data for **c** is provided as a Source Data file.

https://doi.org/10.1038/s41565-024-01681-7

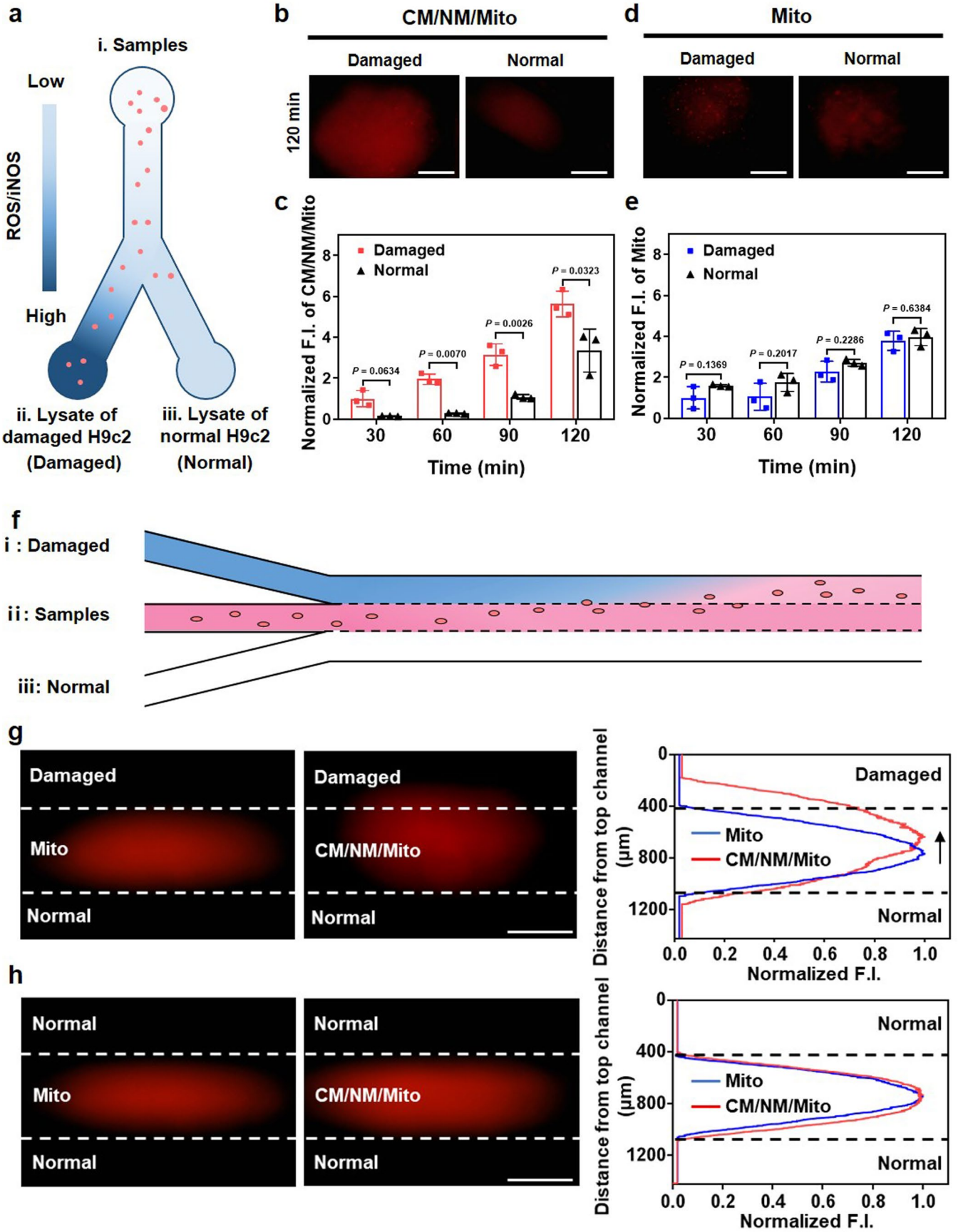

Extended Data Fig. 3 | See next page for caption.

https://doi.org/10.1038/s41565-024-01681-7

Extended Data Fig. 3 | Chemotaxis behaviour of CM/NM/Mito. a. Schematic illustration of the Y channel. **b**-**e**. Fluorescence images (120 min) and corresponding quantitative analysis of the normalized fluorescence intensity in reservoir ii and iii at different time after addition of CM/NM/Mito (**b** and **c**) and unmodified mitochondria (**d** and **e**) (scale bar: 500 μm; n = 3 biologically independent samples). **f**. Schematic illustration of the Ψ microfluidic device. **g**. Fluorescence images and corresponding fluorescence intensity distribution of CM/NM/Mito and unmodified mitochondria in the microfluidic device applying gradient concentrations of damaged H9c2 cell lysate and normal H9c2 cell lysate (scale bar: 500 μm). **h**. Fluorescence images and fluorescence intensity distribution of CM/NM/Mito and unmodified mitochondria in the microfluidic device applying gradient concentrations of normal H9c2 cell lysate (scale bar: 500 μm). Data are presented as means ± SD. Statistical significance was calculated via two-tailed unpaired Student's t test in **c**, **e**.

https://doi.org/10.1038/s41565-024-01681-7

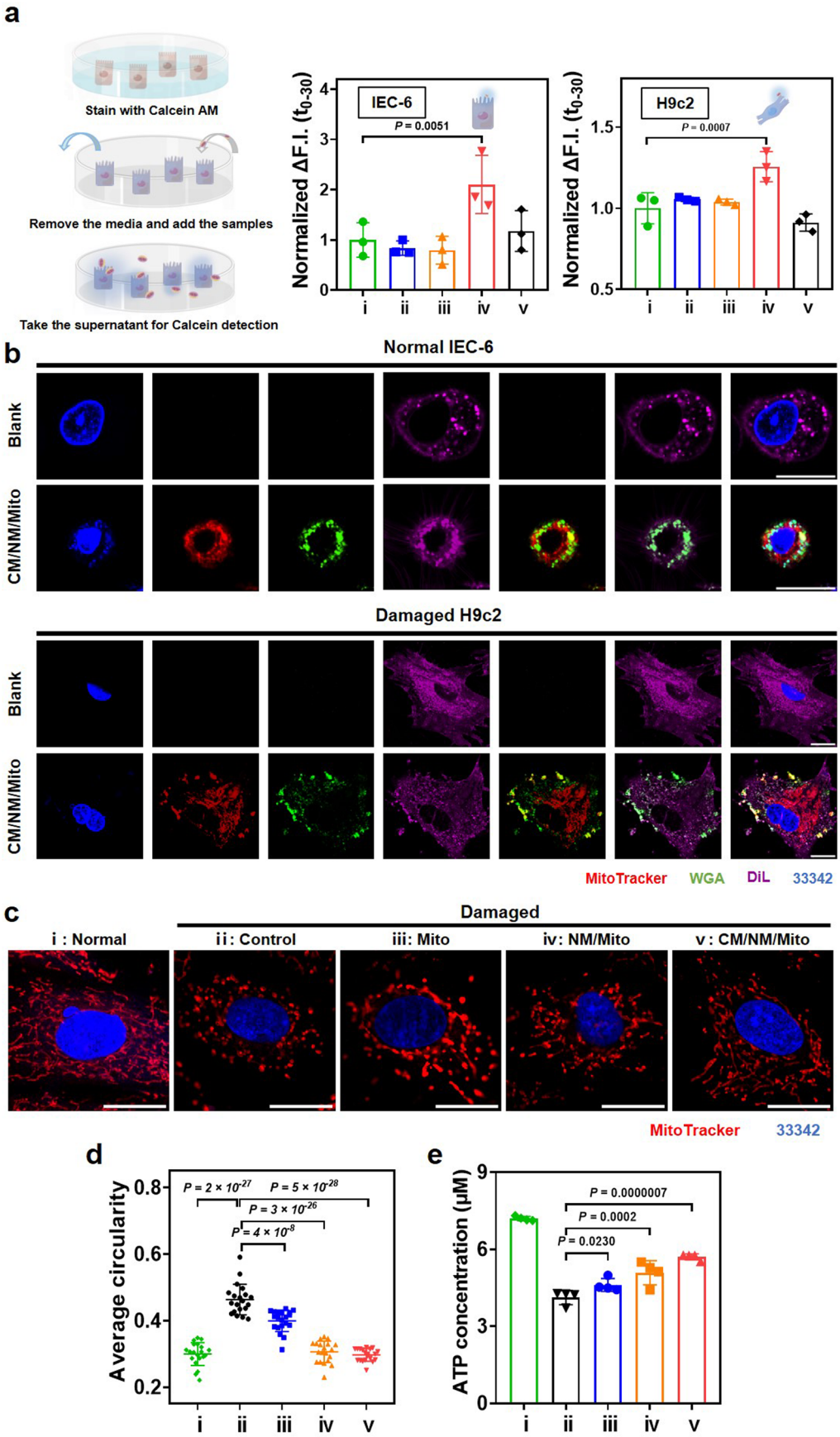

Extended Data Fig. 4 | See next page for caption.

https://doi.org/10.1038/s41565-024-01681-7

Extended Data Fig. 4 | Characterization of GJCs formation, membrane fusion and mitochondrial morphology. a. Calcein AM-stained IEC-6 cells and H9c2 cells were incubated with unmodified mitochondria, NM/Mito, CM/NM/Mito, and CM/NM/Mito + CBX for 30 min, and the fluorescence changes in the supernatants were quantitatively analysed (i: control; ii: unmodified mitochondria; iii: NM/Mito; iv: CM/NM/Mito; v: CM/NM/Mito + CBX; n = 3 biologically independent cell samples). **b**. CLSM images of normal IEC-6 cells and damaged H9c2 cells co-incubated with CM/NM/Mito for 6 h (MitoTracker: NM/Mito component; WGA: CM component; DiL: IEC-6 or H9c2 cell membranes; Hoechst 33342: nuclei; scale bar: 20 μm). **c** and **d**. CLSM images (**c**) and mitochondrial morphology analysis (**d**) of H9c2 cells after co-incubation with different samples for 24 h and stained by MitoTracker (MitoTracker: mitochondria, Hoechst 33342: nuclei; scale bar: 20 μm; n = 20 cells examined over two independent experiments). **e**. Intracellular ATP levels of H9c2 cells co-incubated with different samples (n = 4 biologically independent cell samples). Samples in **c**-**e**: i, normal; ii, control; iii, unmodified mitochondria; iv, NM/Mito; v, CM/NM/Mito. Data were presented as means ± SD. Statistical significance was calculated via one-way ANOVA with two-tailed LSD multiple comparisons test in **a, d, e**.

https://doi.org/10.1038/s41565-024-01681-7

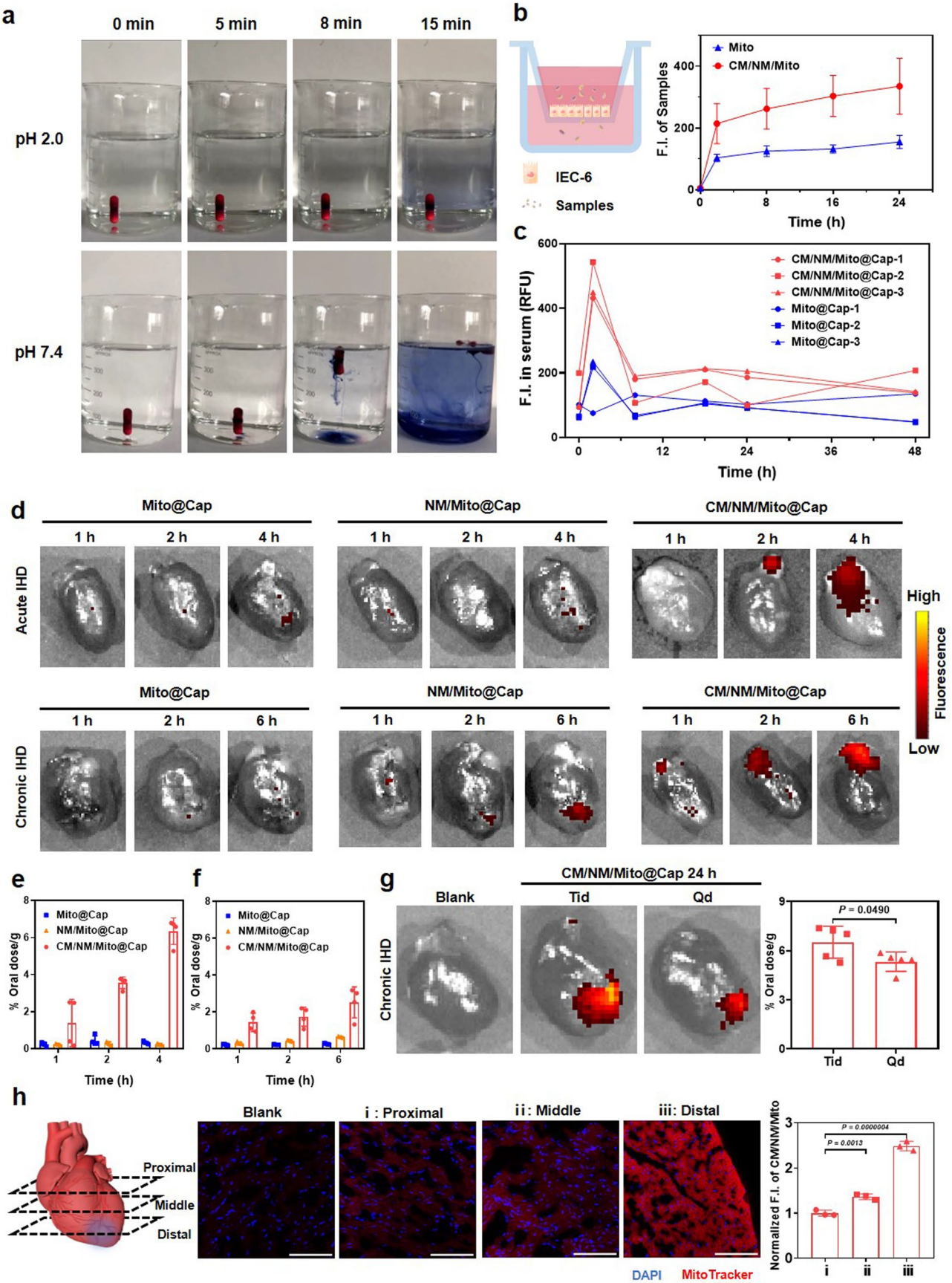

Extended Data Fig. 5 | See next page for caption.

https://doi.org/10.1038/s41565-024-01681-7

Extended Data Fig. 5 | Characterization of pH responsiveness, pharmacokinetics and cardioc delivery efficiency of CM/NM/Mito@Cap. **a**. Disintegration process of large-sized enteric capsules with fuel in PBS with different pH values. **b**. Curve of fluorescence intensity in the lower chamber after adding Mitotracker-labelled CM/NM/Mito or unmodified mitochondira to the upper chamber in the transwell-based intestinal epithelial barrier model. Data were presented as means ± SD (n = 3 biologically independent cell samples). **c**. Curve of fluorescence intensity in serum at different times after administration of Mito@Cap and CM/NM/Mito@Cap in rats (n = 3 biologically independent animal samples). **d-f**. Ex vivo imaging of hearts (**d**) and cardiac delivery efficiency of Mito@Cap, NM/Mito@Cap and CM/NM/Mito@Cap at different time after oral administration of in acute IHD rats (**e**) and chronic IHD rats (**f**) (n = 4 biologically independent animal samples). **g**. Ex vivo imaging of hearts and cardiac delivery efficiency of CM/NM/Mito@Cap (third in die, tid) and CM/NM/Mito@Cap (quaque die, qd) at 24 h after oral administration of in chronic IHD rats (n = 5 biologically independent animal samples). **h**. CLSM images and quantification of fluorescence intensity of cardiac sections at 6 h after oral administration of CM/NM/Mito@Cap in acute IHD rats (i: proximal; ii: middle; iii: distal; MitoTracker: CM/NM/Mito; DAPI: nuclei; scale bar: 100 μm; n = 3 biologically independent animal samples). Data were presented as means ± SD. Statistical significance was calculated via two-tailed unpaired Student's t test in **g** and one-way ANOVA with two-tailed LSD multiple comparisons test in **h**.

https://doi.org/10.1038/s41565-024-01681-7

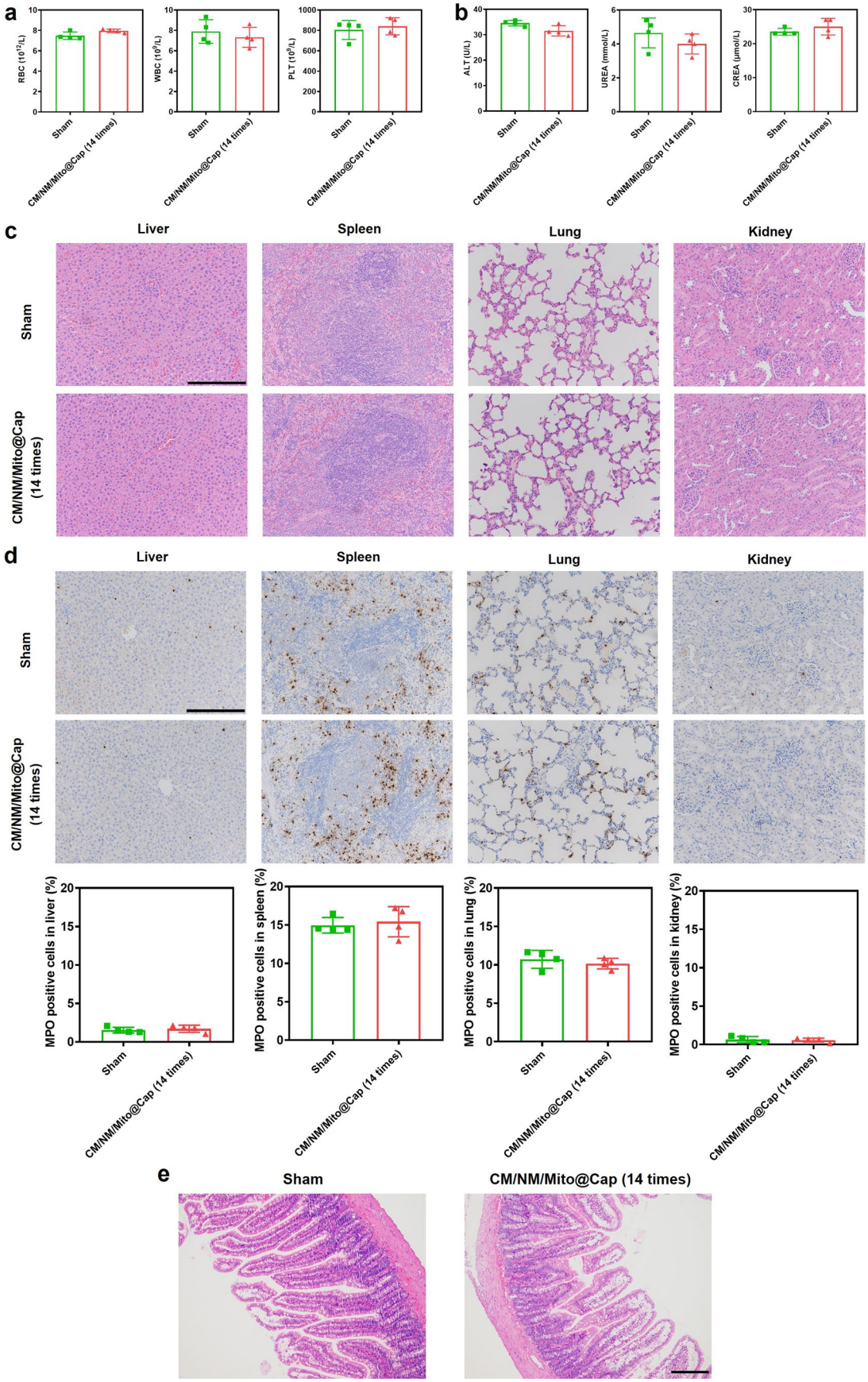

Extended Data Fig. 6 | In vivo biocompatibility of CM/NM/Mito at the end of treatment in the chronic IHD model. a and **b**. Blood routine (**a**) and blood biochemical analysis (**b**) (n = 4 biologically independent animal samples). **c** and **d**. H&E (**c**) and myeloperoxidase (MPO)-immunohistochemical stained main organs and corresponding quantitative analysis (**d**) (scale bar: 200 μm; n = 4 biologically independent animal samples). **e**. H&E stained ileum of rats (scale bar: 200 μm). Data were presented as means ± SD.

https://doi.org/10.1038/s41565-024-01681-7

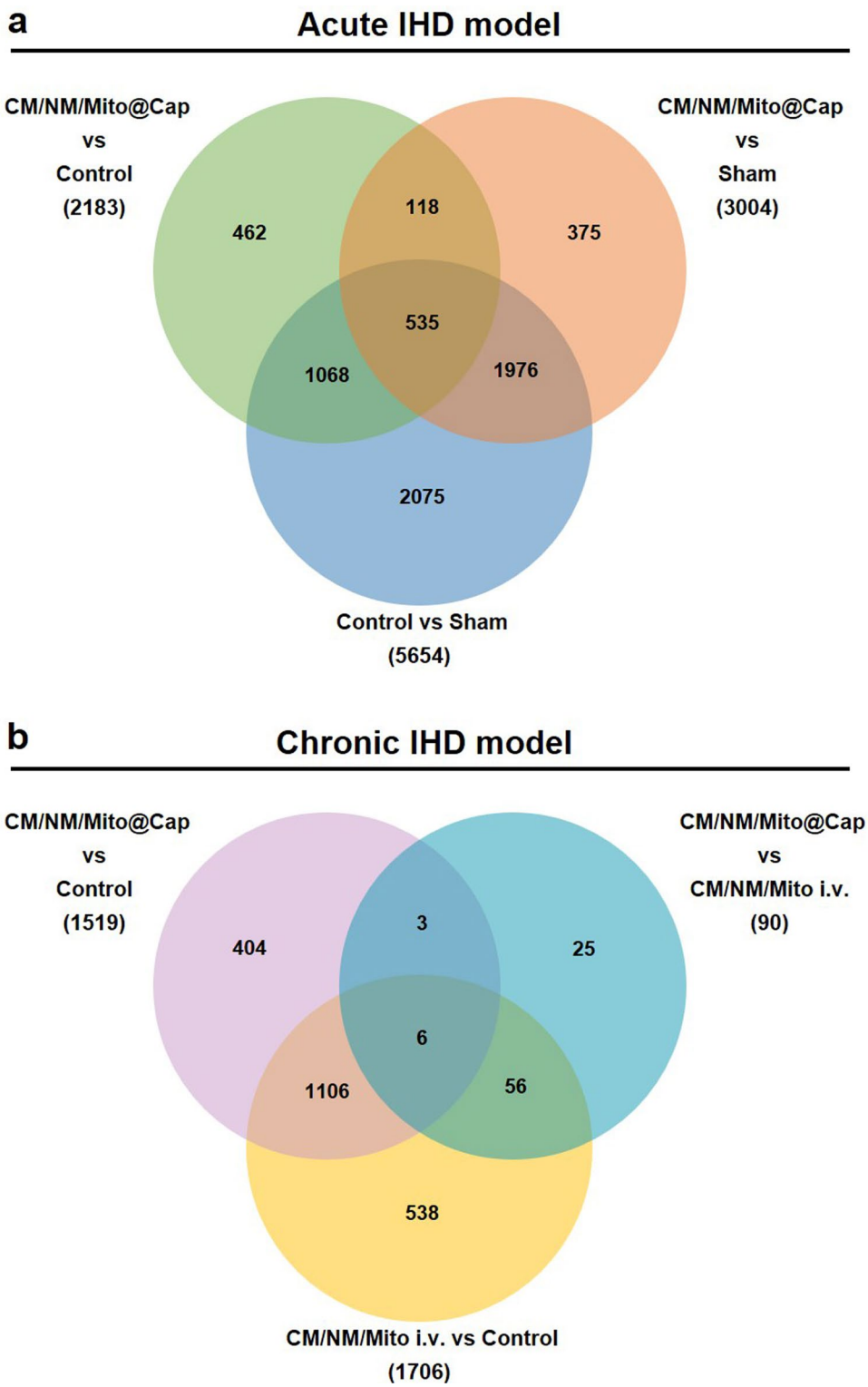

Extended Data Fig. 7 | Transcriptomics analysis in the acute and chronic IHD model. a. Venn diagram for the DEGs detected in hearts after oral administration of CM/NM/Mito@Cap in the acute IHD model (n = 3 biologically independent animal samples in the sham group; n = 4 biologically independent animal samples in the control group and oral administration of CM/NM/Mito@Cap group). **b.** Venn diagram for the DEGs detected in hearts after oral and intravenous administration of CM/NM/Mito@Cap and CM/NM/Mito in the chronic IHD model (n = 3 biologically independent animal samples in per group). The P values were determined using the negative binomial distribution, and then the Benjamini–Hochberg procedure was used for multiple hypothesis testing correction.

https://doi.org/10.1038/s41565-024-01681-7

Extended Data Table 1 | Studies on Mitochondrial Transplantation for IHD

Disease	Donor of mitochondria	Strategy of modification	Route of administration	Research Status	Ref.
IRI	Donor ventricular myocytes	/	Intramyocardial injection	Animal	10
IRI	Autologous pectoralis major muscle	/	Intramyocardial injection	Animal	46
IRI	Human adult cardiac fibroblasts	/	Intracoronary injection	Animal	47
IRI	Autologous pectoralis major muscle	/	Intramyocardial injection	Animal	48
IRI	Autologous pectoralis major muscle	/	Intracoronary injection	Animal	49
IRI	Autologous pectoralis major muscle	/	Intracoronary injection	Animal	50
Heart transplant	Autologous pectoralis major muscle	/	Intracoronary injection	Animal	51
Myocardial ischemia	Autologous pectoralis major muscle	/	Intracoronary injection	Animal	52
IRI	H9c2	Pre-treatment with Alda-1	Intramyocardial injection	Animal	11
Heart failure	Induced pluripotent stem cells	Protection of extracellular vesicles	Intramyocardial injection	Animal	5
Myocardial infarction	Donor heart tissue	Targeting peptide and TPP	Intravenous injection	Animal	63
IRI	Autologous rectus abdominis muscle	/	Intramyocardial injection	Clinical	54
IRI	Autologous rectus abdominis muscle	/	Epicardial injection	Clinical	55

Note: Since 2009, 11 animal studies and two clinical studies have been carried out in the treatment of IHD[5,10,11,46–55]. Conventional open-heart surgery usually involves sawing through the sternum to expose the operative field and establishing extracorporeal circulation if necessary. This procedure is associated with excessive bleeding, significant postoperative pain, and a high incidence of complications such as atelectasis and poor wound-healing[56–59]. Interventional procedure involves the delivery of a catheter to the ischaemic heart through the vessel, and although the invasiveness of the procedure has been reduced, there is still a risk of vascular pathway complications (for example, aneurysm and arterial dissection), as well as coronary complications (for example, coronary spasm and coronary perforation)[60,61]. Furthermore, in addition to being invasive, interventional procedure requires medical devices such as ancillary specialized catheters and guidewires, as well as imaging equipment support. Therefore, we mentioned that the great invasiveness of transplantation method is one of the key reasons limiting the development of mitochondrial transplantation for IHD therapy[11]. On the other hand, for the mitochondria that have been successfully delivered to the damaged heart, some investigators have expressed concern that the viability of exogenous mitochondria may be impaired by the high Ca^{2+} concentrations (~1.8 mM) in the blood or the extracellular fluid in the interstitium, and the ROS in the pathological environment of IHD[7,11]. It has even been suggested that there is no direct evidence that the injected mitochondria remain viable after injection[7,12]. Therefore, we mentioned that the difficulty in maintaining the donor mitochondrial activity in the pathological environment is another key reason limiting the development of mitochondrial transplantation for IHD therapy. This aspect is receiving increasing attention. For example, mitochondrial activity maintenance strategies relying on the protective effect of the cell membrane (extracellular vesicles)[5] and enhancing mitochondrial resistance to oxidative stress[11] have been raised.

nature portfolio

Corresponding author(s): Chun Mao, Min Zhou and Mimi Wan

Last updated by author(s): Apr 10, 2024

Reporting Summary

Nature Portfolio wishes to improve the reproducibility of the work that we publish. This form provides structure for consistency and transparency in reporting. For further information on Nature Portfolio policies, see our Editorial Policies and the Editorial Policy Checklist.

Statistics

For all statistical analyses, confirm that the following items are present in the figure legend, table legend, main text, or Methods section.

n/a	Confirmed	
☐	☒	The exact sample size (*n*) for each experimental group/condition, given as a discrete number and unit of measurement
☐	☒	A statement on whether measurements were taken from distinct samples or whether the same sample was measured repeatedly
☐	☒	The statistical test(s) used AND whether they are one- or two-sided *Only common tests should be described solely by name; describe more complex techniques in the Methods section.*
☒	☐	A description of all covariates tested
☒	☐	A description of any assumptions or corrections, such as tests of normality and adjustment for multiple comparisons
☐	☒	A full description of the statistical parameters including central tendency (e.g. means) or other basic estimates (e.g. regression coefficient) AND variation (e.g. standard deviation) or associated estimates of uncertainty (e.g. confidence intervals)
☐	☒	For null hypothesis testing, the test statistic (e.g. *F*, *t*, *r*) with confidence intervals, effect sizes, degrees of freedom and *P* value noted *Give P values as exact values whenever suitable.*
☒	☐	For Bayesian analysis, information on the choice of priors and Markov chain Monte Carlo settings
☒	☐	For hierarchical and complex designs, identification of the appropriate level for tests and full reporting of outcomes
☐	☒	Estimates of effect sizes (e.g. Cohen's *d*, Pearson's *r*), indicating how they were calculated

Our web collection on statistics for biologists contains articles on many of the points above.

Software and code

Policy information about availability of computer code

Data collection

The surface morphology and dimensions analysis of materials were conducted with a JEM-2100 transmission electron microscope and a 200 kV field emission transmission electron microscope (JEOL JEM-2100F).
Zeta potential and particle size were measured by the Zetasizer (Nano-Z, Malvern, UK).
The particles were counted with a NanoSight NS 300 (Malvern Instruments) high-resolution, real-time dynamic nanoparticle detection technique.
1H-NMR spectra of materials were recorded on a Bruker Avance 400 spectrometer.
The chemiluminescent signal of SDS-PAGE was detected by imaging system (Tanon 5200 Multi).
The fluorescence intensity was detected by a fluorescence spectrophotometers (Hitachi F4600) and a multifunctional enzyme labeling instrument (TECAN Spark).
Cellular ROS and NO was detected by the flow cytometry (BD Accuri C6 Plus flow cytometer).
Fluorescence images of the "Y" channel and the "Ψ" microfluidic device were taken with an inverted fluorescence microscope (MSHOT MF53-N).
Cell imaging was captured using a confocal laser scanning microscope (CLSM, Olympus FV3000).
Calcium imaging for detection of cellular calcium level was recorded using an orthogonal fluorescence microscope (Ningbo YONG XIN Optics Co., Ltd., NE950).
Ex vivo imaging of hearts were acquired and analyzed using IVIS Lumina III, living image system 4.5.5 software.
Echocardiography analysis for detection of cardiac function were performed on a high-frequency high-resolution ultrasound system (VisualSonics, Vevo2100).
The RNA purity was evaluated using a NanoDrop 2000/c spectrophotometer (Thermo Scientific).
R (v 3.2.0) was used to perform PCA analysis, GO and KEGG pathway enrichment analyses and generate the relevant figures.
Quantitative real-time PCR was performed on the QuantStudio™ 6 Flex Real-Time PCR System.

	Metabolic profiling data was acquired using an ACQUITY UPLC I-Class system (Waters Corporation, Milford) and a Q-Exactive quadrupole Orbitrap mass spectrometer equipped with a heated electrospray ionization (ESI) source (Thermo Fisher Scientific, Waltham, MA). The raw data of Metabolomics analysis were processed using Progenesis QI V2.3 software (Nonlinear, Dynamics, Newcastle).
Data analysis	All statistical analyses were performed on Excel (v 2019), SPSS (v 22.0) and GraphPad Prism (v 8). Image J (v 1.54f) was used for fluorescence-image analysis. Pearson's R values were analyzed using the Colco2 plugin for Image J (v 1.54f). Bioinformatic analysis was performed using the OECloud tools at https://cloud.oebiotech.com/task/. FlowJo (v 10) was used for flow cytometry analysis.

For manuscripts utilizing custom algorithms or software that are central to the research but not yet described in published literature, software must be made available to editors and reviewers. We strongly encourage code deposition in a community repository (e.g. GitHub). See the Nature Portfolio guidelines for submitting code & software for further information.

Data

Policy information about availability of data

All manuscripts must include a data availability statement. This statement should provide the following information, where applicable:

- Accession codes, unique identifiers, or web links for publicly available datasets
- A description of any restrictions on data availability
- For clinical datasets or third party data, please ensure that the statement adheres to our policy

The main data supporting the results in this study are available within the paper and its Supplementary Information. There are no data from third-party or publicly available datasets. RNA sequencing data are deposited in NCBI's Sequence Read Archive (SRA) and are accessible through accession number PRJNA1089164 and PRJNA1089186. Raw data of non-targeted metabolomics analysis are deposited in MetaboLights and are accessible through accession number MTBLS9785. All data generated as part of this study are available from the corresponding author upon reasonable request. Source data Fig. 1-5 are available in separate source data files for Fig. 1f-i; Fig. 2d, f, h-k, m; Fig 3f-h, j, l; Fig. 4c, e, g, i-k; Fig. 5g-i, respectively. Source data Extended Data Fig. 1-7 are available in separate source data files for Extended Data Fig. 1b, c; Extended Data Fig. 2c; Extended Data Fig. 2d-g; Extended Data Fig. 3c, e, g, h; Extended Data Fig. 4a, d, e; Extended Data Fig. 5b, c, e-h; Extended Data Fig. 6a, b, d. Source data are provided with this paper.

Research involving human participants, their data, or biological material

Policy information about studies with human participants or human data. See also policy information about sex, gender (identity/presentation), and sexual orientation and race, ethnicity and racism.

Reporting on sex and gender	N.A.
Reporting on race, ethnicity, or other socially relevant groupings	N.A.
Population characteristics	N.A.
Recruitment	N.A.
Ethics oversight	N.A.

Note that full information on the approval of the study protocol must also be provided in the manuscript.

Field-specific reporting

Please select the one below that is the best fit for your research. If you are not sure, read the appropriate sections before making your selection.

☒ Life sciences ☐ Behavioural & social sciences ☐ Ecological, evolutionary & environmental sciences

For a reference copy of the document with all sections, see nature.com/documents/nr-reporting-summary-flat.pdf

Life sciences study design

All studies must disclose on these points even when the disclosure is negative.

Sample size	Sample sizes were determined based on previous studies conducted using similar setups, without the need for additional statistical estimations. To ensure statistical significance, each sample consisted of a minimum of three biological replicates for in vitro studies (Nat. Commun. 2019, 10, 1704; Nat. Commun. 2020, 11, 2549; Nat. Cell Biol. 2023, 25, 989–1003). In the case of in vivo studies, at least three mice were used per group (Nat. Commun. 2022, 13, 6634; Nat. Cardiovasc. Res. 2023, 2, 174–191). The number of samples per group is specified in the figure legends.
Data exclusions	No data were excluded.
Replication	All the experiments have at east three biological replicates. Al the experimental findings were reproducible.
Randomization	Sample allocation was random.

Blinding	Both for in vitro and in vivo studies, the investigators and authors have been consistently blinded to the group allocation during data collection and analysis.

Reporting for specific materials, systems and methods

We require information from authors about some types of materials, experimental systems and methods used in many studies. Here, indicate whether each material, system or method listed is relevant to your study. If you are not sure if a list item applies to your research, read the appropriate section before selecting a response.

Materials & experimental systems

n/a	Involved in the study
☐	☒ Antibodies
☐	☒ Eukaryotic cell lines
☒	☐ Palaeontology and archaeology
☐	☒ Animals and other organisms
☒	☐ Clinical data
☒	☐ Dual use research of concern
☒	☐ Plants

Methods

n/a	Involved in the study
☒	☐ ChIP-seq
☐	☒ Flow cytometry
☒	☐ MRI-based neuroimaging

Antibodies

Antibodies used	anti-Cx43: Connexin 43 Polyclonal antibody (Proteintech, cat. 26980-1-AP (1:1,000 dilution)) anti-Na/K ATPase: Anti-Sodium Potassium ATPase antibody [EP1845Y] - Plasma Membrane Loading Control (Abcam, cat. ab76020 (1:20,000 dilution)) anti-MPO: Recombinant Anti-Myeloperoxidase antibody [EPR20257] (Abcam, cat. ab208670 (1:1,000 dilution)) anti-cTnI: Recombinant Anti-Cardiac Troponin I antibody [EPR20307] (Abcam, cat. ab209809 (1:250 dilution)) anti-CD31: Recombinant Anti-CD31 antibody [RM1006] (Abcam, cat. ab281583 (1:500 dilution)) anti-αSMA: α-Smooth Muscle Actin (D4K9N) XP® Rabbit mAb (Cell Signaling Technology, cat. 19245 (1:500 dilution))
Validation	All antibodies were validated by the commercial supplier. All validation statements can be found on the respective antibody website: anti-Cx43: https://www.ptgcn.com/products/Connexin-43-Antibody-26980-1-AP.htm anti-Na/K ATPase: https://www.abcam.cn/products/primary-antibodies/sodium-potassium-atpase-antibody-ep1845y-plasma-membrane-loading-control-ab76020.html anti-MPO: https://www.abcam.com/products/primary-antibodies/myeloperoxidase-antibody-epr20257-ab208670.html anti-CD31: https://www.abcam.com/products/primary-antibodies/cd31-antibody-rm1006-ab281583.html anti-cTnI: https://www.abcam.com/products/primary-antibodies/cardiac-troponin-i-antibody-epr20307-ab209809.html anti-αSMA: https://www.cellsignal.cn/products/primary-antibodies/a-smooth-muscle-actin-d4k9n-xp-174-rabbit-mab/19245

Eukaryotic cell lines

Policy information about cell lines and Sex and Gender in Research

Cell line source(s)	The rat cardiomyocytes H9c2 (cat. XY-R025) and rat intestinal epithelial cells IEC-6 (cat. XY-R008) were purchased from Shanghai Xinyu Biological Technology. The human umbilical cord mesenchymal stem cells (huMSCs) were provided by Nanjing Taisheng Biotechnology Co., Ltd.
Authentication	The cell lines were not authenticated.
Mycoplasma contamination	All cell lines were tested for mycoplasma contamination. No mycoplasma contamination was found.
Commonly misidentified lines (See ICLAC register)	No commonly misidentified cell lines were used.

Animals and other research organisms

Policy information about studies involving animals; ARRIVE guidelines recommended for reporting animal research, and Sex and Gender in Research

Laboratory animals	Male SD rats (6-8 weeks) weighing 180 g and neonatal rats within 24 h of birth were used. Adult rats were maintained at 21 °C in standard ventilated cages holding 5 rats per cage and water ad libitum.
Wild animals	The study did not involve wild animals studies.
Reporting on sex	Male rats were used for all animal experiments, except for the extraction of primary cardiomyocytes, in which sex-neutral neonatal rats were used.

Field-collected samples	The study did not involve field-collected samples
Ethics oversight	All animal experimental operations were in accordance with the specifications of the Guide for the Care and Use of Laboratory Animals, and all experimental procedures and protocols were approved by the Animal Experimentation Ethics Committee of Nanjing Normal University (approval no. IACUC-20200802).

Note that full information on the approval of the study protocol must also be provided in the manuscript.

Flow Cytometry

Plots

Confirm that:

☒ The axis labels state the marker and fluorochrome used (e.g. CD4-FITC).

☒ The axis scales are clearly visible. Include numbers along axes only for bottom left plot of group (a 'group' is an analysis of identical markers).

☒ All plots are contour plots with outliers or pseudocolor plots.

☒ A numerical value for number of cells or percentage (with statistics) is provided.

Methodology

Sample preparation	H9c2 cells were inoculated in 6-well plates and cultured overnight. Then, normal cells or hypoxia/reoxygenation (HR)-injured cells were co-incubated with CM/NM/Mito (5 × 106 particles mL-1) for another 24 h. The ROS fluorescent probe (DCFH-DA) and NO fluorescent probe (DAF-FM DA) were diluted to 10 μM and 2.5 μM and incubated with the cells for 30 min at 37 °C according to the instructions of the kits (Beyotime Biotechnology, S0033S and S0019). The stained cells were collected and immediately assayed by flow cytometry (BD Accuri C6 Plus flow cytometer). Here, the method causing HR injury in H9c2 cells was as follows: after washed with PBS for several times, cells were put into an Anaeropack hypoxia box (Mitsubishi Gas Chemical Company Inc, 0.1% O2 and 5% CO2) and incubated in the glucose-free and serum-free DMEM for 3 h. Hypoxia-treated cells were then incubated in the complete medium containing glucose and 10% FBS under the atmosphere of 21% O2 and 5% CO2 to realize reoxygenation.
Instrument	BD Accuri C6 Plus flow cytometer
Software	FlowJo (v 10)
Cell population abundance	No post-sort fractions were collected through the Flow cytometry.
Gating strategy	Cells were identified with FSC-A/SSC-A gating and directly followed by the quantitative analysis of mean fluorescence intensity for live cells.

☒ Tick this box to confirm that a figure exemplifying the gating strategy is provided in the Supplementary Information.